Carbon-Based Electrodes for Lithium Air Batteries: Scientific and Technological Challenges from a Modeling Perspective

Alejandro A. Franco[a,b,z] and Kan-Hao Xue[a,b,z]

[a]*Laboratoire de Réactivité et de Chimie des Solides (LRCS) Université de Picardie Jules Verne & CNRS, UMR 7314 Amiens, France*
[b]*Réseau sur le Stockage Electrochimique de l'Energie (RS2E), FR CNRS 3459, France*

The carbon-based positive electrode of Lithium Air Batteries (LABs) is the component where the major competitive mechanisms occur, such as the electrochemical reactions leading to the formation and decomposition of multiple types of lithium oxides, lithium ion and electronic transport as well as oxygen transport. Through a multiscale viewpoint, this review discusses available models describing LAB carbon-based electrodes from the atomistic to continuum approaches. Relevance of those approaches versus experimental data as well as the remaining scientific and technological challenges of these technologies are analyzed. Finally, this review briefly introduces a new theory aiming at studying the impact of the positive electrode carbon structure onto the cyclability of LABs.
© 2013 The Electrochemical Society. [DOI: 10.1149/2.012310jss] All rights reserved.

Types of lithium air batteries.— Advanced electronic equipment and electric vehicle applications have been fast developing, resulting in an ever-increasing demand for high energy density and high power density power sources. Metal air batteries (with metals such as Zn,[1] Na,[2] Mg,[3] and Al),[4] are receiving a growing interest as they theoretically achieve a specific energy significantly higher than current Lithium-Ion Batteries (LIBs) with two intercalation electrodes.[5]

Abraham and Jiang were the first on reporting a practical Lithium Air Battery (LAB) with the use of a Li/C cell in which a gel polymer electrolyte membrane served as both the separator and the ion-transporting medium.[6,7] The theoretical specific energy of their cell was up to ~3400 Wh · kg^{-1}. The reason of such high specific energies is that the positive electrode active material, i.e. oxygen, is not stored internally in the battery. Oxygen actually enters a porous carbon electrode from air for the Oxygen Reduction Reaction (ORR), as a similar functional process to what one has in Polymer Electrolyte Membrane Fuel Cell (PEMFC) cathodes. Lithium and oxygen then react to form metal oxides during the discharge process. During the charge process, the oxides decompose to release lithium ions and oxygen again.

Abraham and Jiang's LAB was actually the first non-aqueous LAB. The operation principle of this kind of LAB is illustrated in Fig. 1. In modern non-aqueous LABs the electrolyte is typically made of lithium salts (e.g. $LiPF_6$) mixed with carbonate-based solvents, such as propylene carbonate (PC), ethylene carbonate (EC) and dimethyl carbonate (DMC), or non-carbonate organic solvents like dimethyl sulfoxide (DMSO). The carbon electrode can support or not catalyst nanoparticles (e.g. RuO_2, Pt, Au, or MnO_2).[8] The resulting positive electrode structure is then inherently multiscale (Fig. 2).

Furthermore, other types of LABs have been the subject of more or less intensive research for the last 15 years, including:

• aqueous LABs consisting of a lithium metal negative electrode, an aqueous electrolyte which contains lithium salts dissolved in water, and a porous carbon positive electrode.[9] In order to avoid the reaction of lithium metal with water, it is required to implement in the cell design a ceramic or glass-like separator between the lithium electrode and the water. Many groups have reported using lithium super-ionic conductors (LISICON, LIPON or LAPT) to act as separator in LABs.[10–12]

• solid state LABs, where the liquid electrolyte is replaced by a solid state electrolyte which is more stable;[14,15]

• aqueous/non-aqueous LABs, being particular in that the electrolyte is divided into two parts, one aqueous (in contact with the

carbon electrode) and the other one aprotic (in contact with the lithium metal electrode), with a lithium-conducting separator (e.g. a ceramic) in between.[16]

Each of those designs has pros and cons. For a good review on the challenges and prospects on both the aqueous and non-aqueous LABs the reader is referred to Christensen et al.[17] At least theoretically speaking, non-aqueous LABs (or simply referred to as LABs in the following) appear to be a good compromise between design simplicity,
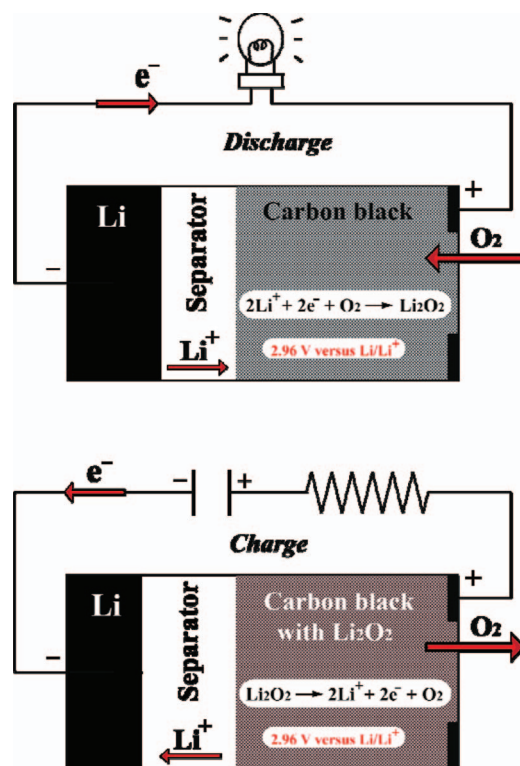

Figure 1. Illustration of the working principles of a non-aqueous LAB. Upper part: discharge operation; lower part: charge operation. The negative electrode is made of a Li foil while the positive electrode is a composite porous electrode consisting of carbon black and binder.

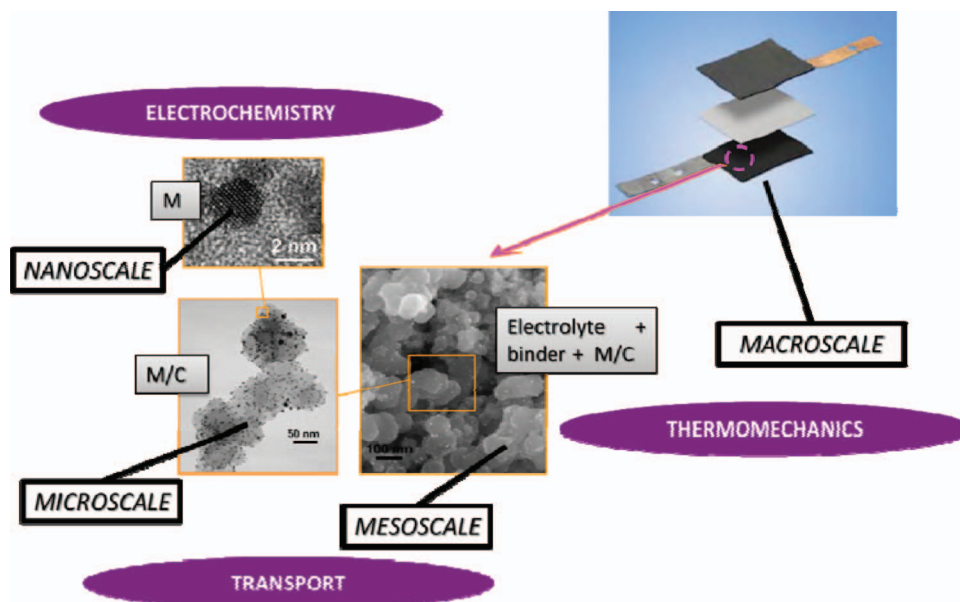[z]E-mail : alejandro.franco@u-picardie.fr; kanhao.xue@u-picardie.fr

Figure 2. A scheme representing the possible multiscale structure of a LAB carbon-based positive electrode. Figure reconstructed from pictures of PEMFC electrode materials in A.A. Franco, *ECS Trans.* **6** (10), 1 (2007).[13]

safety considerations and performance, and they are the main subject of this review paper.

In principle, the use of porous carbon as the active material in LAB positive electrodes appears to be very interesting because it is an inexpensive material. There are however substantial problems in relation with carbon that LABs need to overcome before achieving widespread commercialization. In the following sections, a general overview on the types of carbons currently used, their physicochemical properties and their associated performance and stability properties in non-aqueous LABs will be given.

Porous carbon as positive electrode of lithium air batteries.—
*Types of carbons: general overview.—*The widespread interest and applicability of various carbons in the LAB positive electrodes arises from their high specific surface area, light nature as well as the low fabrication cost. For instance, porous carbons can be seen as defective derivatives of crystalline graphite.[18] Graphite consists of polyatomic carbon sheets (sp^2 hybrid bonding), layer-by-layer, in a hexagonal packed arrangement (i.e. alternating layers in a hexagon unit cell).[19] Porous carbons, such as activated carbons, carbon fibers, carbon blacks and vitreous carbons, are often modeled as disordered arrangements of defective crystallites of graphite.[20]

Up to now, various commercially available carbons, including activated carbon (AC), Vulcan XC-72, Ketjen Black (KB), carbon nanotubes (CNTs), Super P, etc.[21–28] have been employed in LABs. Yang et al. compared the physical parameters and specific capacities of several carbons,[29] as shown in Table I. Among them, AC has the largest surface area (2100 $m^2 \cdot g^{-1}$) but with the lowest reported specific capacity (414 $mAh \cdot g^{-1}$) because of its small pore size (around 2 nm in diameter). In contrast, although with relatively low surface area (62 $m^2 \cdot g^{-1}$), Super P has a high reported specific capacity (1736 $mAh \cdot g^{-1}$),[29] which is due to its larger pore diameter (around 50 nm).

Mirzaeian and Hall were the first to report the synthesis and the use of porous carbon aerogels as positive electrodes in LABs.[30–32] The authors demonstrated that the discharge capacity increases with a larger total pore volume and average pore diameter of the carbon aerogels. Zhou et al. proposed graphene nanosheets (GNS) and demonstrated a comparable electrocatalytic activity for ORR as commercial Pt/C catalyst in a hybrid electrolyte LAB.[33,34] Li et al. then used them in a non-aqueous LAB, exhibiting a discharge capacity of 8705.9 $mAh.g^{-1}$ at a

Table I. Comparison of surface area, pore diameter and specific capacity of various carbons in Yang et al.'s work.[29] Reprinted from L.-L. Zhang, et al., *International Journal of Smart and Nano Materials* 4, 27 (2013).[39]

Carbon material	Surface area ($m^2\ g^{-1}$)	Pore diameter (nm)	Specific capacity ($mAh\ g^{-1}$)
Super P	62	50	1736
Vulcan XC-72	250	2	762
AC[a]	2100	2	414
CNT[b]	40	10	583
Graphite	6	–	560
Ball-milled graphite	480	–	1136
MCF-C[c]	824	30	2500

[a]Activated carbon;
[b]carbon nanotube;
[c]mesocellular carbon foam.

current density of 75 $mA.g^{-1}$. The authors attributed this performance to the structure of GNS, which form a three-dimensional three-phase (solid–liquid–gas) electrochemical interface.[35]

Park et al. have compared the performance of other families of carbons (Fig. 3 and Table II).[36] Among all the employed commercial carbon materials, KB EC600JD appears to be the one with both the largest surface area and pore volume and with the highest specific capacity (2600 $mAh.g^{-1}$). According to this work, both high surface areas and high pore volumes are essential to the high discharge capacity of LABs.

However, we underline that results reported in literature should be analyzed with some precaution as they are difficult to be compared because all the reported works do not use the same electrolytes, and because there is a lack of systematic study on the possible impact of all these types of carbon on the electrolyte degradation. For instance, Park et al. used EC/DMC/EMC for the solvent[36] while Peng et al. used DMSO[37] and replaced carbon by gold for the positive electrode. In addition, Freunberger et al. found no evidence of Li_2O_2 generation in cycling the LAB when alkyl carbonate electrolytes were utilized.[38] Because of dramatic stability issues (discussed later), experiments appear difficult to be reproduced.
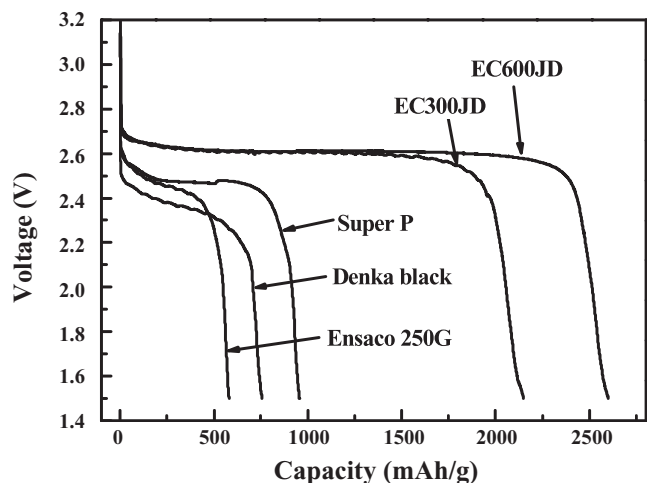
Figure 3. Discharge profiles of Li-air cells with various carbon materials in Park et al.'s research. Figure reprinted with permission from C. K. Park, et al., *Bull. Korean Chem. Soc.* **31**, 3221 (2010).[36]
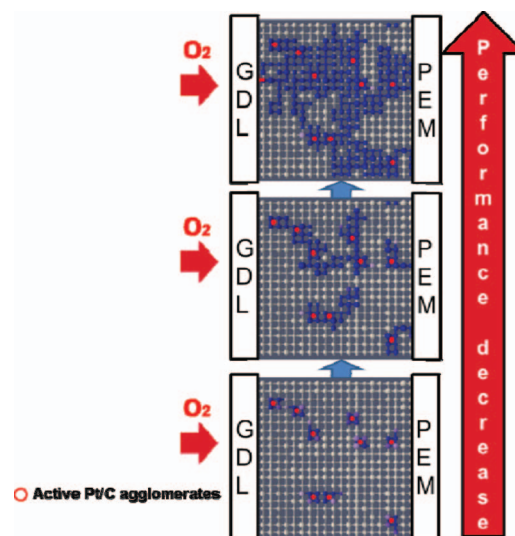

Figure 4. Schematics of the liquid water percolating networks in a PEMFC electrode during its operation (active sites are indicated with red circles). GDL stands for the "gas diffusion layer". Schematics built up with permission by using modeling results on water transport from M. El Hannach, et al., *Electrochim. Acta* **66** (28): p.10796–10808 (2011).

Operation problems.—The performance of LABs has been reported to be affected by many factors such as the air relative humidity,[26] the oxygen partial pressure,[40] the choice of catalysts,[41] the electrolyte composition,[42] the micro- to nanostructure of carbonaceous materials,[24] the macrostructure of the positive electrode,[43,44] and the overall cell designs.[45]

In practice, LABs suffer from poor cyclability (up to few cycles) and reversibility between the discharge and charge (with discharge voltages around 2.5–3.0 V and charging voltages around 4.0–4.5 V).[21,41,46–49] Typical LAB capacity fades twice as fast after 50 cycles (compared to 25% capacity fade after 300 cycles for ordinary LIBs). The high positive electrode polarization (sharp voltage drop-off with increasing current) is frequently believed to be due to the oxygen diffusion limitations. Recent studies have also identified that a possible cause of the high-voltage hysteresis is due to side reactions of the electrolyte with the discharge product of the ORR, Li_2O_2, which can form lithium carbonate and lithium alkyl carbonates with the carbonate species in the electrolyte.[38,50–52] These side reactions are believed to consume the electrolyte during cycling, limiting the reversibility of LABs.

Moreover, O_2 reduction products are mostly insoluble in non-aqueous electrolytes. They precipitate on the surface of the porous carbon electrode.[21,53,54] This ultimately hinders the discharge reaction and also leads to a lower specific capacity than the theoretical value. It has been demonstrated that with the use of some additives in the non-aqueous electrolytes, such as the anion receptor tris (penftaflu-orophenyl) borane, the solubility of solid Li_2O_2 can be dramatically increased, e.g. through the Lewis acid–base interaction between boron and peroxide which enhances the oxidation of solid Li_2O_2 during the charge.[55]

Analogies between discharge in LABs and water generation in PEMFC operation can be done on several aspects. The PEMFC electrode is a porous electrode made of a percolated network of carbon aggregates (of approx. 50 nm size) forming agglomerates which support catalyst nanoparticles (currently Pt) and containing PerFlu-oroSulfonic Acid (PFSA) polymers ensuring proton conduction and the mechanical binding.[13] Thus, the impact of pore clogging on O_2 transport in LAB positive electrodes, can be within some extent as-similated to the impact of liquid water on O_2 transport in PEMFC cathodes. For instance, in low temperature PEMFCs (operation temperatures normally ranging from 25° to 90°C), ORR takes place between e^-, O_2 and H^+ to form H_2O. As the formed H_2O can be in both vapor and liquid phases, transport and pore clogging by liquid water is expected to be strongly dependent on the carbon Pore Size Distribution (PSD), the temperature, and the local reaction kinetics (Fig. 4).[56]

Notwithstanding this similarity, pore clogging by solid oxides in LABs is unfavorable to Li^+ transport whereas pore clogging by liquid water is favorable to H^+ transport in PEMFCs.

It should be noticed that the large majority of experimental data reported in the literature correspond to LAB cells tested with pure O_2. However, within a possible perspective of LAB application in automotive devices for example, the cell is expected to operate with air instead of pure O_2. The LAB positive electrode, if open to the air, can be strongly affected by the environmental conditions. Air breathing from polluted atmospheres (which we can found in most of the cities, with pollutants such as CO_2, NO_x, SO_x, NaCl, O_3, etc.) may strongly affect the cell performance and durability.

Only very few efforts have been reported regarding the impact of external contaminants on the LAB durability. The studies reported concern O_2/CO_2 and O_2/H_2O mixtures. For instance, it has been demonstrated that CO_2 fast reacts with Li_2O_2 resulting in the crystallization of carbonate (Li_2CO_3), which induces an electronic passivation and contributes on clogging the carbon pores and decreasing the overall cell cyclability.[57,58] Moreover, excessive gain of water can dilute the electrolyte.[59] Furthermore, lithium, as most active metals, is unstable in water and may therefore result in self-discharge.

It should be highlighted that it would be important to explore also the impact of mixtures of contaminants, as synergetic or cancellation effects. These mixtures may even mitigate electrode material and electrolyte decomposition, as demonstrated for PEMFCs.[60–63]

Table II. Comparison of surface area and pore volume for various carbon materials, and their influence on specific discharge capacity in Park et al.'s work.[36] Reprinted from L.-L. Zhang, et al., *International Journal of Smart and Nano Materials* **4**, 27 (2013).[39]

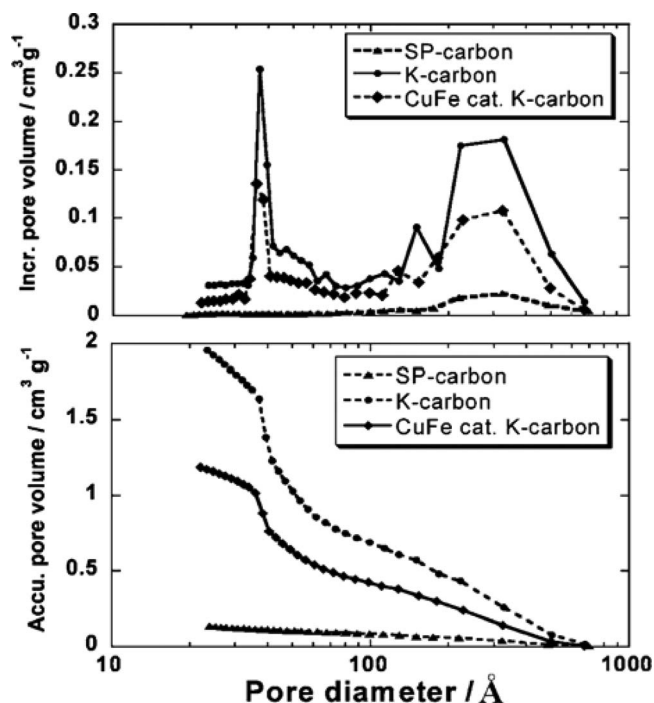| Carbon material	Specific capacity (mAh g^{-1})	Surface area (m^2 g^{-1})	Pore volume (m^3 g^{-1})
KB EC600JD	2600	1325	2.47
Super P	2150	62	0.32
KB EC300JD	956	890	1.98
Denka black	757	60	0.23
Ensaco 250G	579	62	0.18

Figure 5. Incremental (upper) and cumulative (lower) pore volumes as a function of pore diameters in Ren et al.'s work.[22] Three different PSDs were shown, i.e., those of Super P (SP-carbon), Ketjen black EC-600 JD (K-carbon) as well as CuFe-catalyzed Ketjen black EC-600 JD (CuFe cat. K-carbon). Reprinted from Ren et al., *J. Mater. Chem.* **21**, 10118 (2011).[22]

At the best of our knowledge no systematic study has been reported on the impact of these pollutants onto the LAB operation. We should highlight that systematic researches are ongoing to understand the impact of air contaminants on the performance of PEMFCs and it appears to be the way to follow for the case of LABs in not so distant future.[64,65]

Experimental parametric studies on the carbon positive electrode.— It has been reported that the electrode thickness,[43,66,68] the carbon loading[24,43] but most importantly the porosity of the carbon itself,[22,24,29,31,43,44,54,66–69] significantly influence the performance and discharge capacity. The amount of the electrolyte in the air electrode[43] and wettability of the electrolyte[66] have also been reported as important factors. Today, despite some discrepancies, it is mostly agreed that the carbon PSD (and associated surface area and pores volume) is the key parameter governing the LAB performance. Some typical carbon PSDs used in LABs are shown in Fig. 5.

According to Kuboki et al.[44] the pore volume of carbon, rather than its surface area, is the main parameter affecting the discharge capacity. Xiao et al.[43] also showed that the discharge capacity of a LAB was affected by the mesopore volume of carbon, the carbon loading and the electrode thickness. Mirzaeian et al.[31] further reported that a carbon with higher pore volume increased the discharge capacity. Yang et al.[29] also claimed that the surface area was not the only parameter affecting the discharge capacity. According to their results, Super P carbon with a small surface area possessed higher capacity compared to some other carbons with higher surface area. Furthermore, Tran et al. showed[54] that the capacity of the air electrode depended on the surface area of large pores, not the surface area of all pores. They concluded that the micropores and some parts of the mesopores did not play a large role to increase the capacity because they would be blocked by products produced during the discharge reaction. Last but not least, Read[66] studied different types of carbon blacks with a number of electrolytes and suggested that the discharge capacity was related to the surface area wetted by the electrolyte, not to the total surface area of the carbon.
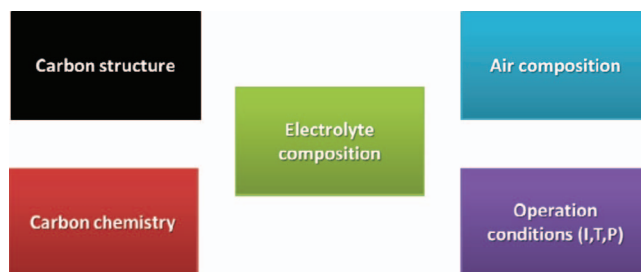

Figure 6. Main factors affecting the performance and durability of Li/C non-aqueous LABs.

It could be expected that the polymeric binder, used in the fabrication process, will have also an impact on the carbon porosity by blocking some of its pores. Younesi et al. carried out experimental studies to investigate how the carbon to binder ratio changes the morphology, surface area, pore volume, and PSD of the positive electrode, and how this affects the discharge capacity of the LAB.[70] The comparison between the different positive electrode films was established by using scanning electron microscopy (SEM), gas adsorption, and electrochemical experiments in combination with three carbonate based electrolytes.

Why modeling?— From the discussion above, summarized with the main factors affecting the LAB performance and durability in Fig. 6, it arises that developing and optimizing the morphology and structure of carbon materials are very important to enhance the performance, safety and durability of LABs.

The optimization of the specific capacity and cyclability of such batteries can be imagined as the optimization of a mathematical merit function in Fig. 7, determined by three factors:

- the intrinsic capacity of the storage materials
- their statistical utilization in the porous electrode
- the macroscopic cell design

Within this sense, physical theory, atomistic/molecular simulation and computational electrochemistry have a crucial role for fundamental understanding, diagnostics and design of new electrochemical materials and operation conditions of LABs. Deep insight based on physical modeling of the materials behavior and aging will advise us how these components with optimal specifications could be made and how they can be integrated into operating devices.

Because of the structural complexity and multi-physics character of LABs, interpretation of experimental observations and ultimate LABs optimization are challenging. An analysis through a consistent multiscale physical modeling approach, in particular consisting of continuum models at the cell level with high predictive capabilities toward the materials atomistic, chemical and structural properties, is required to elucidate the efficiency limitations and their location, the degradation and failure mechanisms.

Despite the impressively increasing number of publications and review papers on LABs,[8,17,71–73] there is as the best of our knowledge still a lack of a review providing an overview of these systems, and in particular with focus on the carbon electrode, from a multiscale modeling perspective. In the following, a critical review on available modeling tools to describe LABs operation is presented. Furthermore, modeling techniques arising from the simulation of LIBs or PEMFCs which could be interesting for the study of LABs are discussed. Then, an innovative multiscale modeling approach being developed by us to understand the carbon structure impact on the LAB performance is presented. Finally, remaining challenges for the modeling of carbon in LABs, as well as LABs in general, are discussed.
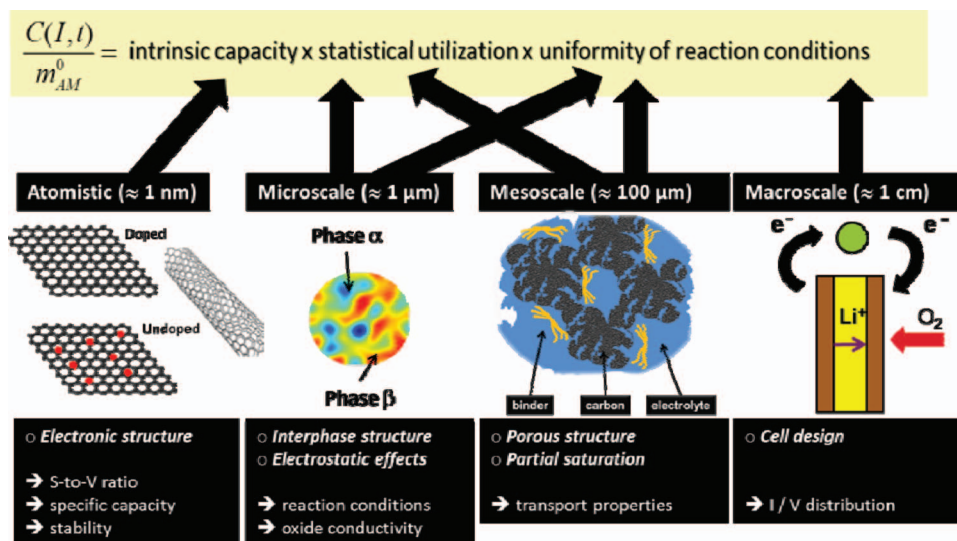
Figure 7. Merit function between scales determining the LAB capacity and cyclability.

Modeling of Carbon in Lithium Air Batteries

Modeling of the carbon-based electrode structure.— In order to understand the mechanical and electrical properties of carbons it is necessary to develop satisfactory models of their structure. Several modeling works have been devoted to understanding the structure of amorphous carbons since the 1980s.[74]

The carbon-based electrode is a multi-composite electrode with a multiscale structure resulting from carbon, binder and electrolyte, and closely related to the fabrication process (solvent used, etc.).

The importance of having a good representation of the electrodes structure is that averaged parameters can be determined by microscale resolved models that are directly describing the morphological structure and aging-induced temporal topological changes. Within this case, as demonstrated for PEMFC modeling but still not applied for LABs, microstructures can be generated *in silico* by stochastic methods (e.g., Monte Carlo-based description of the carbon agglomerates distribution in the electrode, or simpler stochastic electrode reconstruction),[75] atomistic methods (e.g. Coarse Grain Molecular Dynamics – CGMD)[76] or by using experimentally determined structures (e.g. TEM 3D-tomography).[77]

On the basis of these structural predictions, the transport properties of chemical species (e.g. O_2) and of charge (effective conductivities for Li^+ and electrons) can be derived. This allows the assessment of parameters such as the overall electrical conductivity, and the surface area of mutual contact of catalyst and electrolyte particles arranged in different interpenetrated percolating networks. The dependence of these parameters on volume fractions, layer thickness, and size of electrolyte and catalyst particles can be studied.

For example, within this context, CGMD simulations of a PEMFC electrode has been used by Malek and Franco to build a structural database for electrodes with different C contents in terms of interpolated mathematical functions describing the impact of the C mass loss (induced by corrosion) on the evolution of the ionomer coverage on Pt and C, the electronic conductivity of the CB, the C surface area and the Pt surface area (which re-organizes during the C corrosion process).[78] These functions are then integrated into a cell model to simulate the impact of C corrosion on the Membrane-Electrodes Assembly performance decay (Fig. 8). CGMD methods, which are actively researched in a large number of application areas, combine units of the material into larger fragments (called "beads"), which can be modeled efficiently using law-timescale methods, such as Brownian dynamics. Parameterization of the interactions of these units requires feedback from atomistic simulations. The details on this methodology for performing studies of self-organization in PEMFC electrodes mix-

tures have been described by Malek et al.,[79] where they represent all atomistic and molecular species, i.e., Nafion ionomer chains, solvent molecules, water, hydronium ions, carbon and Pt particles, by spherical metallic, polar, nonpolar, and charged beads with pre-defined sub-nanoscopic length scale.

A similar methodology would be very relevant to understanding the influence of the carbon microstructure, in relation with the electrode fabrication method, on the LAB performance. Analogous modeling approaches are being developed to understand ionic transport inside carbon nanopores for supercapacitor applications.[80]

Modeling of the carbon reactivity.—Ab initio studies of carbon reactivity toward the ORR and the Oxygen Evolution Reaction (OER).— While carbon has been widely used as the positive electrode material for LABs, it is still unclear what role carbon plays in the ORR (discharge) and in the OER (charge). The experimental data on the carbon reactivity toward ORR and OER are very rare, perhaps because carbon has been regarded as not very active in this reaction. The first theoretical investigation on this issue in relation with the ORR was carried out by Xu and Shelton,[81] who did ab initio density functional theory (DFT) calculations on the adsorption of Li, molecular oxygen, various Li_xO_y as well as CO_x groups on the surfaces of several model graphitic carbon structures (see Fig. 9 for various minimum energy configurations). They first found that molecular O_2 does not adsorb on graphite (0001) surface, and the perfect graphite (0001) surface has strong resistivity against oxidization. This implies that the reduction of O_2 depends on some associative channels, such as LiO_2 and LiO_2Li where Li is also present. Secondly, the intermediates LiO_2 and LiO_2Li molecules are highly mobile on graphite (0001) surface, with a high probability to enter a different phase, i.e., the electrolyte or solid agglomerates. Thirdly, the armchair-type edge and carbon vacancies are highly reactive, leading to carbonate and lactone groups, respectively, after oxidization. Finally, the existing CO_x functional groups are active in Li oxidization. Overall, those carbon atoms lacking of covalent bonds, as well as existing CO_x functional groups show high activity for ORR by Li.

In another study, Xiao et al.[82] studied the adsorption of Li_2O_2 monomers on graphene substrates by DFT. They found only slight adsorption if the graphene substrate is perfect, similar to the previous study by Xu and Shelton. However, the binding energy of Li_2O_2 monomers near defect sites is much stronger, and even stronger if both defects and COOH groups are present. Therefore, their study implies that the positive electrode structure of a LAB can be optimized through the adjustment of defects and functional groups on the graphene sub-
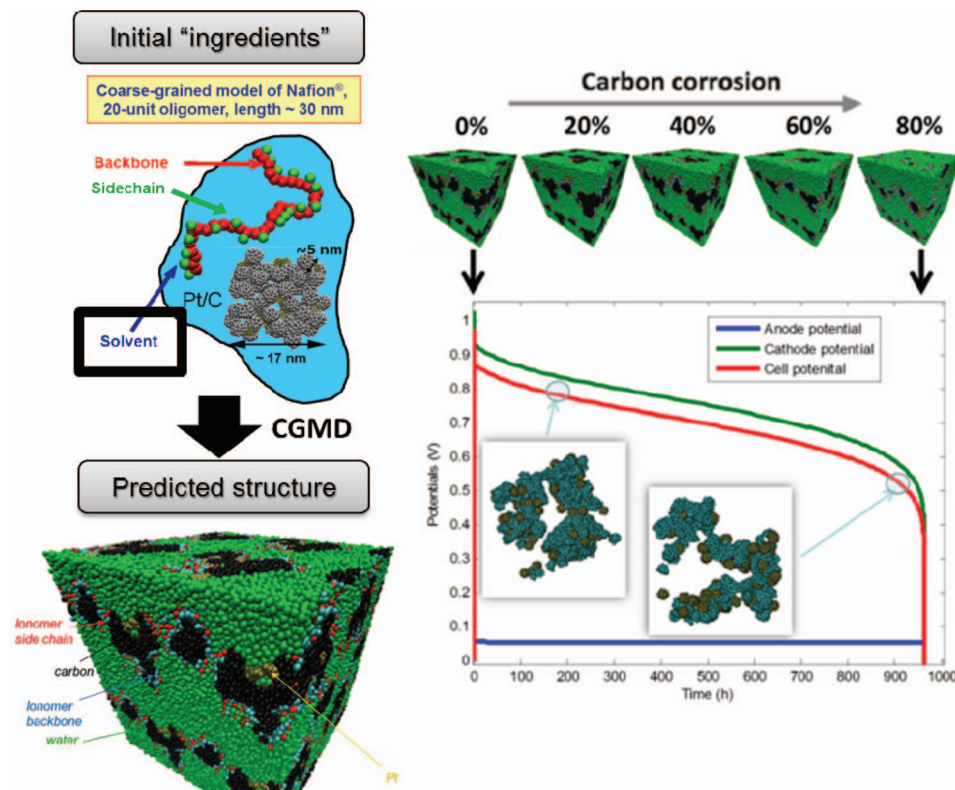
Figure 8. Coarse Grain Molecular Dynamics model of cathode carbon corrosion in PEMFCs. Figure reconstructed from K. Malek and A. A. Franco, *J. Phys. Chem. B* **115**, 8088 (2011).[78]
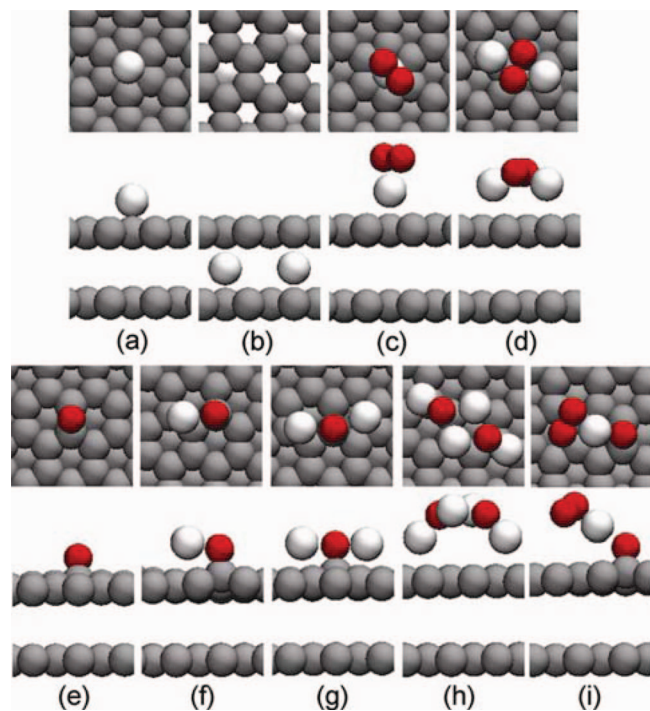

Figure 9. Calculated minimum energy geometries for Li-O species on graphite (0001) surface by Xu and Shelton.[81] (a) adsorbed Li; (b) intercalated Li; (c) LiO_2; (d) LiO_2Li; (e) O; (f) LiO; (g) Li_2O; (h) $(Li_2O)_2$ and (i) LiO_2 near an O. Reprinted from Y. Xu and W. A. Shelton, *J. Electrochem. Soc.* 158, A1177 (2011).

strate. They proposed a novel approach using hierarchical porous functionalized graphene sheets (FGS) as the positive electrode of LAB, where the FGS material contains a certain amount of oxygen. In this way an extremely high discharge capacity, 15000 mAh/g was achieved, as shown in Fig. 10. In particular, the discharge products Li_2O_2 did not aggregate; instead, they formed isolated nanosized islands, which prevented pore clogging and electronic passivation. This experiment supports the viewpoint that by optimizing the morphology of carbon, a good reactivity in the positive electrode chemistry can be achieved in LABs even without additional catalysts.

Finally we underline that any study available in literature reporting Nudged Elastic Band (NEB) calculation results[83] is very helpful for understanding the kinetic properties of carbon toward the ORR, such as previously demonstrated within the community of PEMFCs.[84]

Reactivity of catalyst-decorated carbon toward the ORR and the OER: available DFT studies.— In order to reduce the positive electrode overpotentials, the use of metal oxides or metal nanoparticles as ORR (discharge)/OER (charge) electrocatalysts has been suggested.[21,23,41,46,85] There is, however, still controversy on the real impact of these electrocatalysts on the LAB operations. For instance, McCloskey et al. demonstrated that the gas evolution related to electrolyte solvent decomposition was the dominant process being catalyzed.[86] According to these authors, in an electrolyte where Li_2O_2 formation is the dominant product of discharge, no catalytic activity, compared to pure carbon, is observed using Au, Pt or MnO_2 nanoparticles, therefore conventional OER electrocatalysis may be unnecessary.

Among the theoretical investigations based on quantum mechanics, DFT is the method largely used to study the catalytic properties of
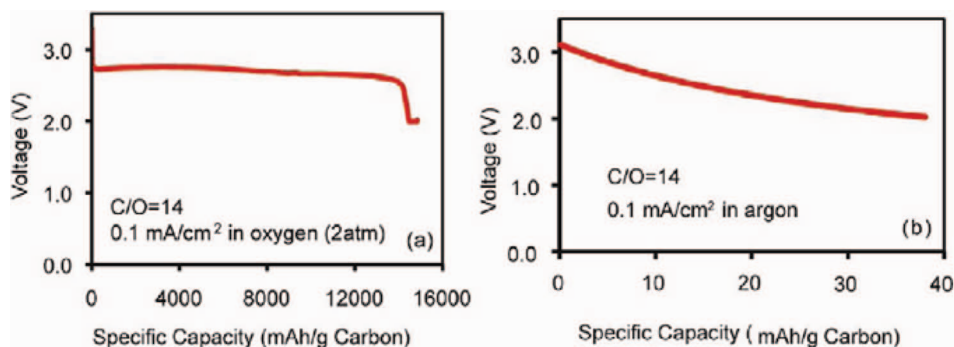
Figure 10. Discharge curves of the cells in Xiao et al.'s work[82] using FGS as the positive electrode of the LAB. (a) C/O ratio is 14 and oxygen pressure is 2 atm; (b) the same cell as in (a) but tested in pure argon. Reprinted with permission and with abridgment from Xiao et al., *Nano Lett.* **11**, 5071 (2011).

PEMFC catalysts. The exploration of those properties has been carried out by using different models and conditions, from clusters composed of a few metallic atoms to extended surfaces, and from vacuum to solvated conditions, with or without external electric field.[87–95]

Franco et al. developed a multiscale model allowing simulating the impact of the chemical and structural properties of the catalyst nanoparticles onto the effectiveness of the ORR under a large diversity of PEMFC and PEM Water Electrolyzers operation conditions.[84,96–99] The model is developed within a Mean Field framework describing the elementary kinetic steps of the ORR, competing adsorption and desorption of reaction intermediates O_2, O, OH, OOH, H_2O, H_2O_2, and the interfacial catalyst/electrolyte charge transfer (H^+, e^-) effects. The elementary kinetic steps in the model have been parameterized by activation barriers extracted from DFT calculations carried out on both 2D Pt and Pt_xM_y periodic slabs, with M being a transition metal element. NEB approach is for instance employed in order to calculate the activation energies of each single elementary reaction (E_{act}), which are further implemented in Eyring's equations allowing for the expression of the kinetic parameters. The model also includes a dynamical description of the structure of the electrochemical double layer (EDL), able to predict the local proton transport as function of the reaction conditions, in particular regarding the morphology of the PFSA (Nafion) polymer at the vicinity of the catalyst: the description of this is crucial as it is expected that Nafion adsorbs on the catalyst with a coverage depending on the catalyst charge density, reducing the ORR effective activity as recently demonstrated by experimentalists.[100] Experimental observables (cyclic voltammetry, electrochemical impedance spectroscopy, polarization curve) can thus be calculated.[101]

At the best of our knowledge there is still a lack of literature on theoretical studies of the ORR and OER on catalyst surfaces in particular relation with LABs. The effect of non-aqueous solvent and the different cations (Li^+ instead of proton) make the reaction mechanism on the catalysts in LABs different from the PEMFC case. Further efforts are necessary within this direction.

Modeling of transport process within the carbon based electrodes.—Electronic transport in the carbon network.— Not all crystalline carbons are electronic conductors. On the one hand, diamond is an insulator because each carbon atom forms covalent bonds with its four neighbors, in sp^3 hybridized orbitals. On the other hand, in graphite, planar graphene sheets consist of unsaturated sp^2 orbitals that account for its conductivity. Nevertheless, carbon definitely shows conductivity in its amorphous forms. For example, amorphous carbon black particles consist of mainly sp^2 orbitals but with minor sp^3 orbitals,[102] thus they are highly conductive.

Structural studies show that carbon black primary spherical particles (radius usually ranging from 10 nm to 100 nm) mainly consist of concentrically oriented graphene layers.[103] Hence, electronic conductivity inside the primary particles is very high. During the fabrication process, many primary particles are usually fused together to form

aggregates.[104] Within the same aggregate, some graphene layers extend across two primary particles, therefore reducing the interconnection resistance between the particles. Figure 11 illustrates the primary particles and aggregates in carbon blacks, where a particle is spherical but the shape of an aggregate is usually like a chain (Fig. 11b).

In the positive electrode of LABs the aggregates are bound together to form agglomerates. One can view, electronically, the aggregates as the individual units to build up the porous electrode because of the high conductivity within each aggregate. The main resistance of a carbon black porous electrode comes from the interconnection between different aggregates. Nevertheless, even this resistance is too low to be considered as significant (ranging from 0.1 to 10 S/cm).[104]

The true resistance in the positive electrode comes from the discharge products on top of the carbon black surface, Li_2O_2/Li_2O, since they are insulators as bulk materials. Nevertheless, in real situations a finite conductivity may still emerge due to defects, grain boundaries or surfaces. A detailed understanding of the conductivity within the resulting lithium oxides requires the ab initio calculation techniques.

While the crystal structure of Li_2O is simply a cubic anti-fluorite structure (Fig. 12; space group: *Fm3m*), there are various models proposed for Li_2O_2: one proposed by Féher et al. in 1953[106] (space group: $P\bar{6}$), another one proposed by Föppl in 1957[107] (space group: $P\bar{6}$), and a higher-symmetry model (space group: $P\bar{6}_3/mmc$) proposed by Cota and de la Mora in 2005[108] through first-principles calculations. The $P\bar{6}_3/mmc$ model (shown in Fig. 12) can basically be regarded
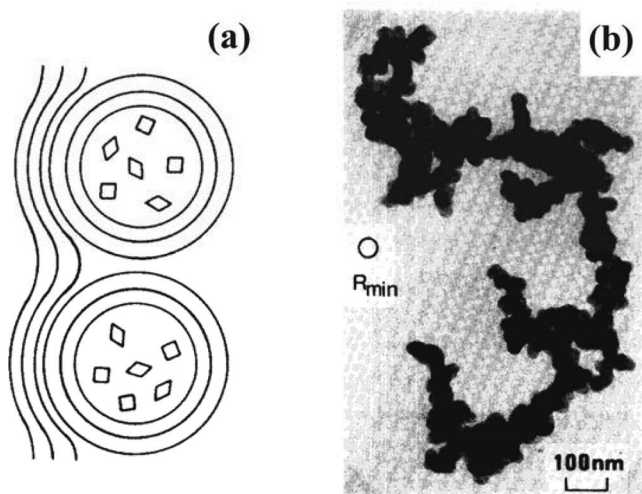

Figure 11. (a) Schematic view of two carbon black particles in an aggregate; (b) Transmission electron microscopy of a carbon black aggregate. Reprinted with permission from J. Lahaye and F. Ehrburger-Dolle, *Carbon* **32**, 1319 (1994).[105]
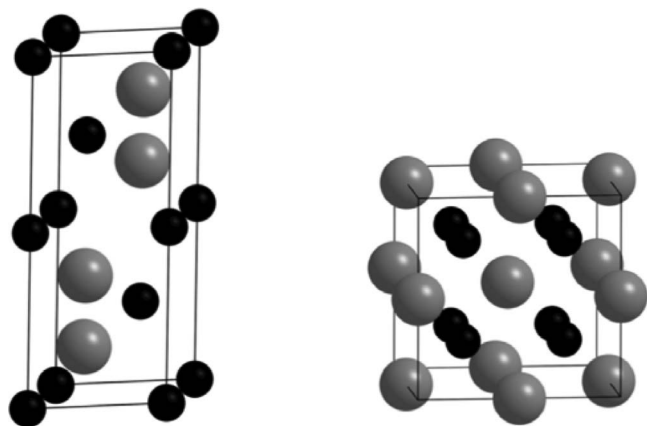
Figure 12. Schematic crystal structures of (left) bulk Li_2O_2 and (right) bulk Li_2O. Small, black balls represent Li while big balls represent O. Reprinted with permission from M. D. Radin, J. F. Rodriguez, F. Tian, and D. J. Siegel, *J. Am. Chem. Soc.* **134**, 1093.

as a high symmetry version of the Föppl model. Later, Chan et al.[109] showed both experimentally and computationally that the Föppl model is a better representation of Li_2O_2 than the Féher model. Recent first-principles calculations usually adopt the high-symmetry $P\bar{6}_3/mmc$ model.[110,111]

Radin et al.[111] performed first-principles calculations on various Li_2O_2 and Li_2O surfaces, and found that the two lowest energy surfaces of Li_2O_2 are oxygen-rich $\{0001\}$ surface and oxygen-rich $\{1\bar{1}00\}$ surface. The former one is the most energetically favorable. Calculations on these two surfaces reveal that both of them are half-metallic. A half-metal is a magnetic conductor where only one electron spin component shows conduction while the other spin component does not.[112] In contrast, the most energetically favorable Li_2O surface is stoichiometric $\{111\}$, which is insulating. Hence, it was concluded that in LABs Li_2O_2 surfaces are metallic but Li_2O surfaces are not. A later publication of the same group[113] used several different methods such as DFT with generalized gradient approximation (GGA) using the Perdew-Burke-Ernzerhof (PBE) functional,[114] Heyd-Scuseria-Ernzerhof 2006 (HSE06) hybrid functional[115,116] and GW approximation[117] (both G_0W_0 and self-consistent GW), and concluded that the bulk bandgap of Li_2O_2 should lie between 5.15 eV (G_0W_0 result) and 6.37 eV (self-consistent GW result). Moreover, all methods confirm the half-metallic nature of the oxygen-rich Li_2O_2 $\{0001\}$ surface.

Aside from the oxygen-rich surface conduction argument by Radin et al., there are also researchers reporting hole polaron hopping conduction in Li_2O_2. Considering the electrons in the O-O bond of peroxides are highly localized, Ong et al.[118] discovered that holes introduced in Li_2O_2 are trapped in the $\pi*$ anti-bonding molecular orbitals of the O-O bond, forming polarons because the trapped holes can modify the O-O bond strength to cause significant local distortion. However, even if the holes are trapped, the resulting polaron hopping barriers are merely 68 meV for intra-layer hopping and 152 meV for inter-layer hopping. Moreover, the holes are strongly bound to Li vacancies if they exist, and electronic conduction is highly related to vacancy diffusion. Garcia-Lastra et al.[119] further confirm the localization of electrons and holes in Li_2O_2, resulting in electron polarons and hole polarons. Yet, only hole polarons have a small hopping barrier, while electron polarons suffer from more than 1 eV hopping barrier. They further concluded that neither *n* type nor *p* type doping in Li_2O_2 is effective in improving its conductivity, because of the localization behavior of carriers that forbids a band conduction mechanism.

Albertus et al.[120] also performed first-principles calculations on the electronic structures of Li_2O, Li_2O_2 and Li_2CO_3 using the GW approximation. The calculated band gaps for the three bulk materials are 7.44 eV, 5.12 eV and 8.83 eV, respectively.

Compared with theoretical calculations, experimental measurement of the conductivity in Li_2O_2 is relatively rare. Very recently, Gerbig et al.[121] conducted the first systematic experimental study on defect chemistry and conduction in Li_2O_2. They found that Li_2O_2 is mainly an ionic conductor with 10^{-10}-10^{-9} S/cm bulk ionic conductivity at 100°C while the electronic conduction contribution is much smaller, 10^{-12}-10^{-11} S/cm at 100°C. This confirms the extremely low electronic conductivity in this material, as can be the main hindrance to the discharge capacity of LABs.

The published results up till now tend to support the fact of a very bad electronic conductivity in Li_2O_2. Even though the surface conduction scheme by Li vacancy has been proposed and supported by the presence of reversibility in Li_2O_2 but not in Li_2O, it is still worthwhile to note that the sudden death of a LAB may occur when the thickness of Li_2O_2 film formed within the positive electrode is still less than 5 nm, as reported by and proposed as a question to the surface conduction scenario by Garcia-Lastra et al.[119] This leads to the question whether bulk conduction is hard to achieve but only thin film Li_2O_2 could be tolerated such that electron tunneling may occur.

On the computational side, the critical point regarding the relative stability of surfaces with various stoichiometries strongly depends on the calculation error on oxygen molecule binding energy. It is a well-recognized fact that DFT/GGA gives an incorrect oxygen molecule binding energy, which is defined as the energy of an isolated oxygen molecule subtracting twice the energy of an isolated oxygen atom. Since in LABs O_2 is the active species to be adsorbed or released, the chemical potential of the excess/missing oxygen on the surface is crucial to the stability of non-stoichiometric surfaces. Several approaches exist in the literature to overcome this insufficiency of DFT/GGA. Wang et al.[122] suggested a +1.36 eV correction to the oxygen molecule energy calculated by GGA-PBE functional, which is based upon the correct formation enthalpy of various oxide materials. On the other hand, Radin et al. used a +0.86 eV correction to their oxygen molecule energy derived from GGA-PBE, which ensures a correct binding energy of oxygen molecule. Note that the plane-wave cutoff energy used in their Vienna *Ab-Initio* Simulation Package[123,124] (VASP) code is 400 eV. In other calculations with the same code and same pseudopotentials, a 500 eV plane-wave cutoff energy[118] as well as a 275 eV cutoff energy[125] were also utilized. In order to better compare different calculation results, affording supplementary information such as the dependence of oxygen molecule energy on plane-wave cutoff energy is strongly recommended. In addition, it is pointed out by many authors that none of the present calculations have considered the role of the electrolyte solution on the solid surface, and calculations with this effect included are very necessary, as the next step of computational study. Last but not least, the electrical properties of Li_2O_2 or Li_2O grain boundaries have not been theoretically investigated yet. While Radin et al. mentioned that the grain boundaries in Li_2O_2 may be conductive, this suggestion is not justified yet and specific grain boundary models for Li_2O_2 need to be set up. In other polycrystalline wide-gap oxides such as HfO_2, some theoretical studies indeed reveal possible metallic conduction along the grain boundaries, due to either oxygen vacancy segregation[126,127] or metal interstitial incorporation.[128]

As the effective electronic conductivity through the lithium oxide layer depends on the formation, segregation and percolation of the different and more or less conductive phases, it is important to understand the microstructural evolution of the layer upon discharge and charge. The microstructure resolution would determine how the oxide layer morphology impacts the electronic conductivity and associated polarization of the ORR/OER (Fig. 13).

In the case of LAB models reported in literature, the oxide thickness growth is assumed to increase the electronic resistivity through empirical mathematical expressions, without any link to detailed chemistry of the oxide particles or layers. Phase field modeling approach constitutes an elegant way of capturing the formation and the evolution of the solid oxide phases as a function of the LAB operation conditions. The phase field modeling approach is now receiving a growing attention to understand phase separation, until now mainly
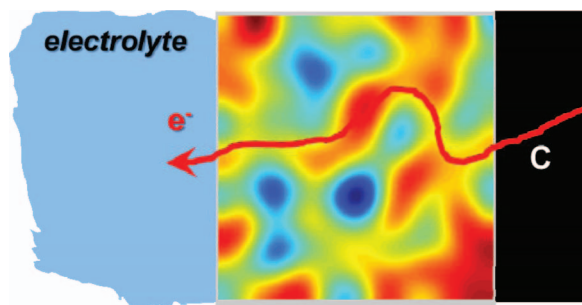
Figure 13. Schematics of the phases percolation and favorite electronic conduction pathway through a lithium oxide layer.

on LiFePO$_4$ materials in lithium ion batteries.[129–131] Phase field models allow moving beyond traditional Fick's law in describing solid phase diffusion. They are potentially more accurate, and allow simpler tracking of phase boundaries than Fick's equation. The phase field modeling approach was initially developed for describing phase separation and coarsening phenomena in a solid[132] and later for electrochemistry applications.[133–135] Within this approach, we consider in our theory the total Gibbs free energy of the oxide particle or layer, as follows:

$$G = \oint_V \left(g_{bulk} + g_{grad} + g_{app} \right) dV + \oint_V \oint_{V'} [g_{non\,local}] dV\,dV' \quad [1]$$

where g_{bulk} is the local chemical Gibbs free energy density (function of the composition in each phase), g_{grad} is the gradient energy density (accounting for the heterogeneities penalties, with parameters such as the interphase energies which can be evaluated from ab initio calculations), g_{app} is the coupling potential energy between the applied fields and order parameters, and the second integral accounts for the long range interactions. The chemical potential of each phase is given by

$$\mu_j = \frac{\partial G}{\partial c_j\,(\vec{r},\,t)} \quad [2]$$

and the conservation equation governing the phases formation and displacement is given by

$$\frac{\partial c_i}{\partial t} = -\vec{\nabla} \cdot \vec{J} = \vec{\nabla} \cdot \left(M_{ij} \vec{\nabla} \mu_j \right) \quad [3]$$

where M_{ij} refers to the mobility of each phase (could depend on the phases concentrations). Equation 3 is known as the *Cahn-Hilliard* equation[136] and its numerical solution will provide the structural evolution of the lithium oxide phases during discharge and charge. Some ongoing work under this direction is in progress by us and will be reported in a later publication.[137]

On the experimental side, experimental examination of the conductivity of Li$_2$O$_2$ {0001} surface is very much required. Specifically, it was reported by different authors that the stoichiometric surface and the oxygen-rich surface are the most energetically favorable surface configuration, respectively.[111,125,138] Experimental clarification of this issue is important.

Lithium ion transport in the electrolyte: continuum modeling.— In LAB modeling, there are two sorts of transport involved. First, Li$^+$ transport within the electrolyte phase of the cell occurs back and forth between the negative electrode and the positive electrode. Secondly, oxygen molecules flow from the environment to the active pores in the positive electrode during discharge and are expelled from the pores during charge.

For the Li$^+$ transport part, the problem looks very similar to the LIB case. Indeed, since the first models proposed by Newman's group on lithium battery in 1993[139] and on LIB in 1994,[140] numerous attempts exist to attack the lithium ion transport problem in the electrolyte solution. There are multiple theories with different foundations. To

clarify the problem, we imagine here a very ordinary case where there are only one sort of cation, Li$^+$, only one sort of anion, X$^-$ (X can be PF$_6^-$, ClO$_4^-$, etc.), and only one sort of solvent in the electrolyte solution. The molar concentrations of the cation, the anion and the solvent are denoted by c_+, c_-, and c_0, respectively. In order to set up the proper material balance equations that can be coupled with current-potential equations, the first task is to properly reduce the number of concentration variables such that the number of unknown concentration variables equals that of the material balance equations. In the past many modeling work on Li$^+$ transport in LIBs, there are three general approaches classified by the above criterion:

1. The coupled Poisson-Nernst-Planck equation approach. This is the approach used for example in Lai and Ciucci.[141,142] It treats the transport of each species as independent, and the influence of the solvent is embodied in the permittivity term of the Poisson's equation. Two Nernst-Planck equations are required (as well as two Poisson's equations) in order to model the transport of the cation and the anion, respectively. This approach reduces the number of concentration variables from 3 to 2. Yet, since the cation and the anion are treated separately, it involves two Nernst-Planck equations to account for the material balance of both charged species. A great benefit of this approach is that it allows for the charge separation, therefore may be useful for the regions close to or inside the EDL of the electrodes. Moreover, it also allows for coupling to microscopic modeling such as DFT calculations.[143] The drawback lies in that it regards the movement of species as independent and thus cannot describe concentrated solutions.

2. The concentrated solution theory[144] used by Newman's group in LIB models.[139,140] A main feature of this theory is that it does not separate the cation transport from the anion transport. Nor does it neglect the role of solvent. In order to reduce the number of concentration variables, the first step is to assume the electroneutrality condition, where only one of the two charged species' concentrations is needed and the other's concentration is automatically derived from the electroneutrality condition. The second step utilizes the Gibbs-Duhem equation to eliminate the electrochemical potential of one of the three species, while the electrochemical potentials are related to their corresponding concentration variables. This approach is suitable for the concentrated solution case, since it is based on a multicomponent transport equation where the driving force for one species also depends on all other species. Also, it allows the consideration of convection.[145] Yet, in its current form, the strict electroneutrality condition forbids its application to the EDL region at the interface between the active materials and the electrolyte. Further extension of the theory beyond electroneutrality is recommended.

3. Latz's approach[146] which, accepting the electroneutrality condition, eliminates explicitly the second concentration variable by a strict convection-free condition. This approach is based on linear irreversible thermodynamics where the entropy production term comes from a hydrodynamic theory of electromagnetic fields in fluids developed by Henjes and Liu,[147] and also Liu.[148] There is one implicit assumption in this theory, that the partial molar volume ratios can be approximated by molar mass ratios among all species. This assumption is the basis of the convection-free equation in the theory, and it together with the definition of partial molar volume further leads to a constant solution density within the cell. It is well-known that during discharge, the salt concentration is higher in the negative electrode but lower in the positive electrode, thus the solution density is not in general uniform. The quality of this assumption depends on the particular salt and solvent used in the cell. In addition, the electroneutrality restriction also forbids its application to the EDL region.

The original model by Newman's group uses concentrated solution theory partly because the salt concentration in the electrolyte of a lithium ion cell is usually between 1M and 2M, as a rather concen-
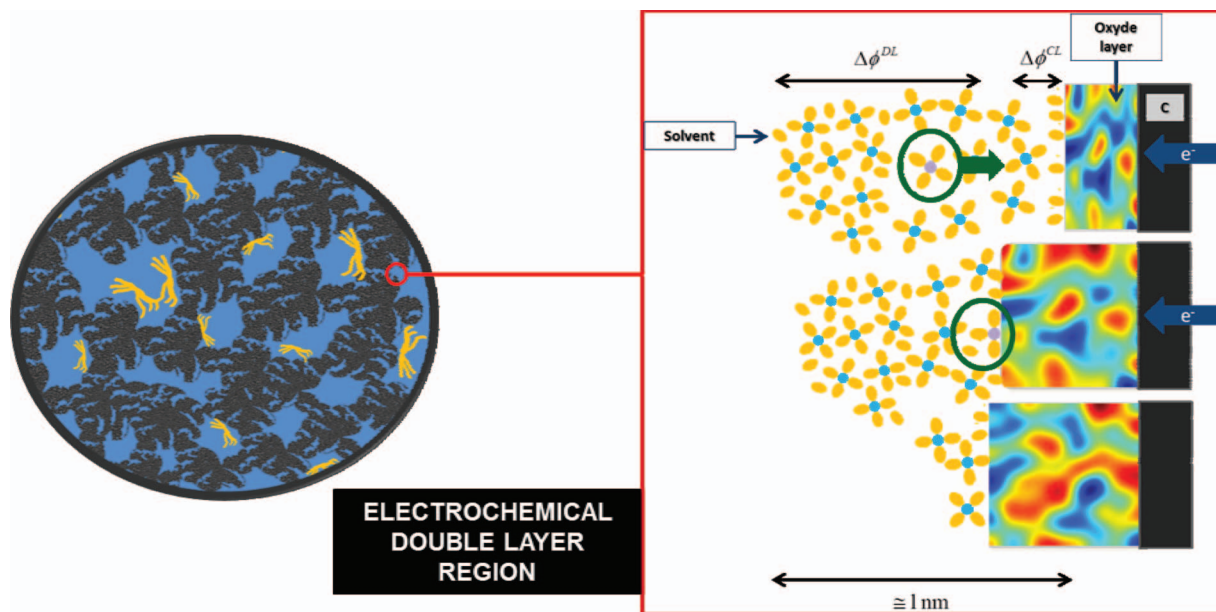
Figure 14. Schematics of the Li$^+$ transport within the EDL region at the interface between the lithium oxide layer and the electrolyte. Two polarizations are speculated to impact the polarization of the ORR and the OER: one associated to the diffuse layer and the other one to a compact layer formed by solvent molecules adsorbed on the oxide layer.

trated solution. In addition, the high conductivity of the concentrated solution renders the EDL region very narrow. This justifies the use of electroneutrality condition in modeling the electrolyte phase transport of a LIB.

Nevertheless, LAB is different from LIB in several critical aspects. First, Li$^+$ reacts directly with O$_2$ and electrons to generate several discharge products on top of the positive electrode particles in a LAB, where the EDL region is always adjacent to the reaction sites. In contrast, in a LIB Li$^+$ intercalates into the solid particles across the EDL region, but will further diffuse away from the EDL region. This discrepancy ought to be considered in applying the LIB theories to LABs. Secondly, the detailed reaction chemistry depends critically on the electrode surface in LABs, which renders the study of the EDL region significant. Thirdly, the volume expansion of the positive electrode in a LAB during discharge is enormous, though the global volume change of the cell is to a much less extent. In particular, the Li negative electrode is quickly consumed in volume since Li is a very light metal. Hence, there can be a relatively constant flow of the electrolyte solution from the positive electrode to the negative electrode during the galvanostatic discharge of a LAB, which implies that the even the velocity of the solvent cannot be simply set to zero with respect to the cell body. Last but not least, the discharge/charge rate of LAB is usually very low due to (i) the amount of dissolved oxygen in the electrolyte solution is very limited; (ii) the discharge products are usually insulating, severely limiting the rate of electron transfer. Hence, the Li$^+$ concentration is not supposed to vary much during cell operations. It may also be not necessary to use a very concentrated solution. Even when the ionic conductivity is taken into account, a 0.5 M[149] or 0.1 M[49] solution seems to be sufficient in LABs rather than 1 M in LIBs.

Considering these new characteristics in the Li$^+$ transport in LAB, we can envisage some different strategy from the LIB modeling. First, whenever a less concentrated solution is used, the coupled Poisson-Nernst-Planck equation approach can be beneficial since it accepts the permittivity as a parameter coming from ab initio calculations. Secondly, since the electrode kinetics is both complex and significant for modeling, inclusion of an explicit treatment of the EDL region in the model is appealing. This requires going beyond the electroneutrality condition at least in the EDL region. The EDL modeling should in particular capture the impact of the electrolyte composition onto the

interfacial Li$^+$ transport and compact layer formed by the adsorption of solvent molecules on the oxide layer, as well as the associated electrolyte/solid polarizations (Fig. 14). We underline that this is still a question theoretically unsolved even for LIBs. Some work is in progress by us on this topic and will be published later.[150] Thirdly, a convection velocity considering volume changing of both electrodes during cell operations need to be retained or added in the transport equations.

Another key problem is to consider the porous structure of the carbon electrode. The material balance equation mentioned above, regardless of which approached adopted, usually involves diffusion, migration and convection terms of Li$^+$. Nevertheless, in a porous electrode some modifications should be done, for example, to the diffusion term. The effects of porosity and tortuosity in diffusion have been widely modeled in LIBs by a Bruggeman relation:

$$D^{eff} = \frac{\varepsilon D}{\tau} \qquad [4]$$

or

$$D^{eff} = \varepsilon^p D \qquad [5]$$

where D^{eff} is the effective diffusion coefficient, D is the diffusion coefficient measured in pure solutions, ε is the porosity, τ is the tortuosity and p is the Bruggeman coefficient.[151] In the LIB literature p is usually taken to be 1.5, though some modeling works use experimental discharge/charge curves to fit a best value of p.[152] The porosity is usually treated as constant, expect for one paper by Sikha et al.[153] who accounted for the volume change of the porous electrodes in a LIB. Nevertheless, in LABs the volume change of the carbon positive electrode is significant during cell operation, where a variable porosity must be considered. Hence, the kinetic rate of discharge product generation is coupled back to the Li$^+$ transport equation through the dynamic porosity term. Moreover, pore clogging due to the discharge products is a common phenomenon in LABs, which may decrease the available porosity to an even lower value than expected. Modeling of pore clogging and investigation into different PSDs is an essential work to be carried out in LABs.

Oxygen transport in the electrolyte: continuum modeling.— Compared with Li$^+$ which is in abundance, the very low solubility of
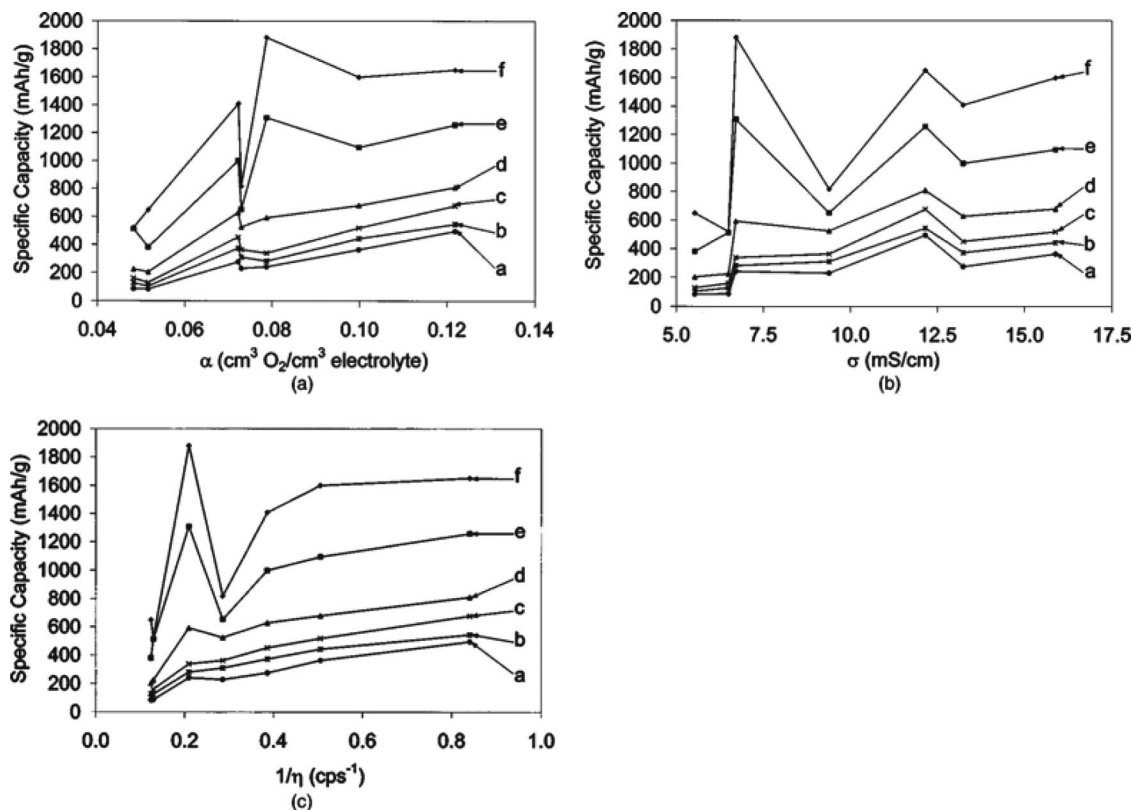
Figure 15. Variations of specific capacities of a LAB cell from Read et al. with: (a) Bunsen coefficient α; (b) electrolyte conductivity σ; (c) inverse of viscosity η. Reprinted from *J. Electrochem. Soc.*, **150**, A1351 (2003).

oxygen makes oxygen transport in the positive electrode of LABs a key rate-limiting factor during discharge.[154] It must be emphasized here that there are two different carbon positive electrodes: the fully electrolyte-flooded electrode and the partially wetted gas diffusion electrode. The former is a two-phase system with oxygen dissolved in the electrolyte phase, but the latter is a three-phase system, i.e., a carbon black solid phase, an electrolyte phase and a gaseous phase. While only one porosity is involved in the former, two porosities characterizing both the electrolyte phase and the gaseous phase volume fractions, should be introduced in the latter. Most of the existing positive electrodes in the literature, however, are fully electrolyte-flooded.

On the methodology side, current LAB models on fully flooded positive electrodes treat the oxygen transport as Fickian diffusion.[120,155–159] Since oxygen molecule is electrically neutral and is rather dilute in organic electrolyte solutions, this approach seems to be the most natural one. Moreover, oxygen is regarded as the only gaseous species in this treatment, which is consistent with the widely adopted experimental scheme of a Li-oxygen battery. An experimental support of a Fickian diffusion mechanism comes from Read et al.,[155] who measured the impact of oxygen Bunsen coefficient and viscosity of the solvent, as well as the conductivity of the electrolyte on the discharge capacity of a LAB. The results of Read et al. are shown in Fig. 15, where from (a) and (c) it is demonstrated that the Bunsen coefficient α (representing the oxygen concentration in the electrolyte) and the viscosity η have strong influence on the discharge capacity. Instead, in Fig. 15b the specific capacity is shown to be generally insensitive to the electrolyte conductivity, as long as the conductivity is not very low. On the one hand, the oxygen concentration is proportional to the Bunsen coefficient[160]

$$c_{O_2} = \frac{n_{O_2}}{V} = \frac{\alpha p_{O_2}}{RT} \quad [6]$$

where c_{O_2} and n_{O_2} are the molar concentration and amount of substance for oxygen in the solution, respectively; p_{O_2} is the partial

pressure of oxygen in the environment; V is the volume of the solution; R is universal gas constant; and T is the absolute temperature. On the other hand, the viscosity η of the solvent is related to the diffusion coefficient D of oxygen by the Stokes-Einstein relation

$$D = \frac{k_B T}{6\pi \eta r} \quad [7]$$

where k_B is Boltzmann constant and r is the radius of the species that is subject to diffusive motion. Therefore, the trends in Figs. 15a and 15c highlight the Fickian diffusion as governing the law of oxygen transport, while the Li$^+$ transport is less important.

Contrary to the Fickian diffusion, as the pore size becomes tens of nanometers Knudsen diffusion may dominate. While Fickian diffusion characterizes the collision between gas molecules, Knudsen diffusion considers the case when the mean free paths of individual gas molecules are much longer than the dimension of the pores in a porous electrode, such that gas molecules mainly interact with the solid pore walls. This is indeed the case in the primary pores of a LAB carbon positive electrode, if they are not yet clogged by the discharge products. The Knudsen diffusion term can be added to the Fick's law or the Stefan-Maxwell transport equation. The latter case is also named as the Stefan-Maxwell-Knudsen equation that has been applied in fuel cell modeling.[84]

If a Li-oxygen battery becomes a Li-air battery, a direct impact would be the lowered partial pressure of oxygen gas. According to Henry's law, the dissolved oxygen in the electrolyte will become 20.95% of the original value. This will bring about great performance limitation due to the reduced available oxygen content close to the active surfaces of the positive electrode. Another point deserving attention is the contaminant components such as water and CO_2. Hence, in the case of a real Li-"air" battery, it is possible that the Stefan-Maxwell formalism of the multi-component transport,[161] rather the Fickian diffusion, is more suitable in modeling the oxygen transport.

The pore clogging phenomenon is important for LABs, because it has been reported by Tran et al.[54] that the micropores and some of the mesopores are subject to full clogging at the early stage of discharge. On the other hand, Albertus et al.[120] reported only 2%-3% volume of the positive electrode occupied by the discharge products and concluded that pore clogging is not the dominant limitation in the LAB cells. It deserves attention that the carbon material used by Tran was high surface area carbon but that used by Albertus et al. was Super P, which has large pores and small surface area ratio. It is known mathematically that at the same mass a porous carbon with a smaller average pore size has a larger surface area, therefore the average pore size in the experiment of Albertus et al. is assumed to be larger than in that of Tran et al. Such may be a reason accounting for the different conclusions regarding pore clogging. Indeed, in LABs low surface area ratio carbon materials such as Super P, may show larger discharge capacity compared with fine pore carbon materials (Table I). This is in contrast to fuel cells and aqueous LABs where the discharge products are soluble, such that high surface area carbon materials are preferred.

The proposal of oxygen diffusion electrode provides another challenge for oxygen transport in LAB modeling. Tran et al.[54] optimized the structure of a 3D oxygen diffusion electrode where a considerable gas volume exists near the gas inlet. Xia et al.[162] recently proposed that a carbon positive electrode completely flooded with electrolyte tends to restrict the oxygen diffusion; therefore a partially-wetted positive electrode can be helpful in solving this problem. Their experimental results (shown in Fig. 16) show that the partially-wetted carbon positive electrode shows a discharge capacity of 4200 mAh/g, much larger than a conventional flooded electrode which shows 2600 mAh/g discharge capacity. If the partially-wetted positive electrode is going to become the state-of-the-art technology, modeling of the oxygen transport must take into account the gas phase of oxygen or air. In particular, since the transport occurs in a porous media, within the gas phase it is possible to have Darcy transport. The difference between the Darcy mechanism and Stefan-Maxwell as well as Knudsen mechanisms are summarized by Pisani[163] as follows. A given species may lose momentum through:

• Stefan-Maxwell: transfer to another species as a result of collisions between pairs of unlike molecules.
• Knudsen: direct transfer to the pores walls through particle-wall collisions.
• Darcy: indirect transfer to the wall via a sequence of molecule-molecule collisions terminating in a molecule-wall collision.

Whole cell models.— Before discussing the published continuum-scale whole-cell models on LAB, we first notice two models for specific purposes. Read et al.[155] were the first to model a LAB cell (in 2003), where they used the Stokes-Einstein relation to estimate the diffusion coefficient of oxygen in the electrolyte solution, employing the experimental viscosity data. Based on a Fickian diffusion mechanism they were able to simulate the oxygen concentration profiles during discharges. The results show that the oxygen concentration in the positive electrode region close to the separator drops significantly during discharge. Zheng et al.[164] in 2008 estimated the gravimetric and volumetric energy densities of aqueous and non-aqueous LABs, considering the porosity of the positive electrode. However, these two models do not involve the simulation of the discharge or charge I-V curves of the cell.

The first comprehensive model of a LAB is from Sandhu et al.[156] in 2007, who assumed that the influence of lithium transport is trivial and considered an oxygen diffusion-limited isothermal model. This is justified both because the discharge/charge rate is low, and because the 1M concentration of Li+ is sufficient to avoid salt depletion. Hence, the Li+ concentration can be conveniently taken as 1M everywhere and all the time. The oxygen transport follows Fick's law as well as a continuity equation, and the kinetic rate of electrode reaction during discharge was taken approximately as linearly dependent on the oxygen concentration. In this approximation, a Tafel kinetics was

used, but the power of oxygen concentration is exactly 1, regardless of the asymmetric factor. Cylindrical pore geometry was assumed, and pore volume change due to discharge products was considered. It was assumed that the discharge products (Li_2O_2) are insoluble, thus a linear relation exists between pore volume and the generated Li_2O_2.

In 2010, Andrei et al. proposed a model[157] similar to that of Sandhu's, but the transport of Li+ was considered using the concentrated solution theory by Newman.[144] In particular, the diffusion conductivity of the electrolyte solution was included, and the material balance equation is the same as that of the standard LIB model.[140] The Bruggeman exponent was introduced to modify the effective values of the diffusion coefficient and the electrolyte conductivity in porous media. For the oxygen transport part, a Fickian diffusion equation together with a continuity equation was utilized, similar to previous modeling works. For the electrode kinetics, still a linear relation between the oxygen conversion rate and the oxygen concentration was assumed, similar to Sandhu et al. However, a Butler-Volmer kinetics was used, instead of the Tafel form.

Albertus proposed a physics-based continuum-scale model for LAB in 2011.[158] Different from previous models, they assumed the discharge products are mainly Li_2CO_3 because a carbonate solvent, PC, was used in their experimental study. Regarding the Li+ transport, concentrated solution theory was used, similar to the standard LIB model. A Fickian diffusion was adopted as the transport mechanism of oxygen, and the porosity was assumed to vary linearly with
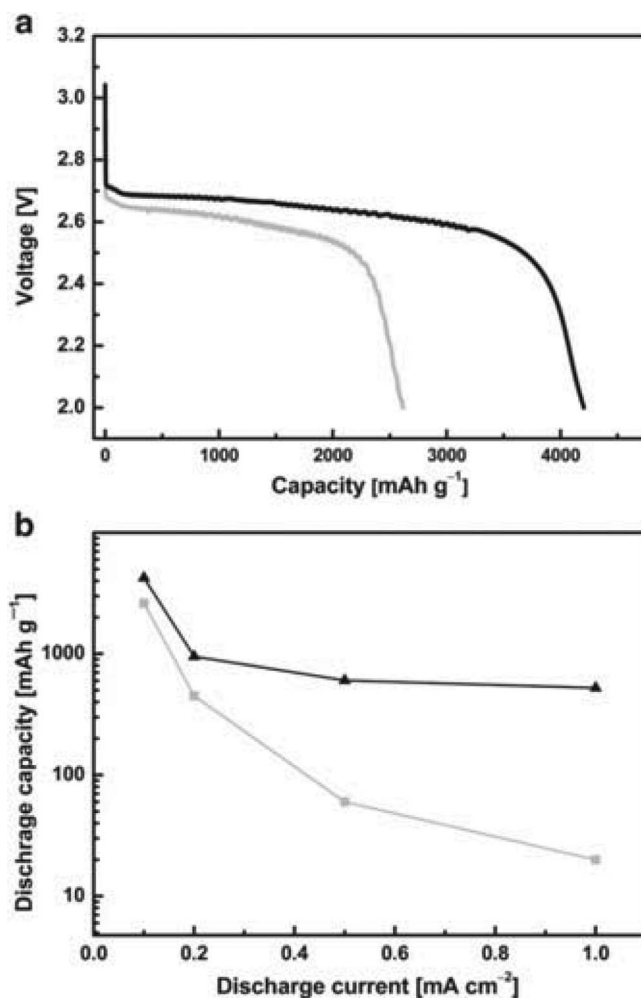

Figure 16. (a) The discharge curves of a LAB cell with a flooded positive electrode (gray) and a partially-wetted positive electrode (black) at 0.1 mA · cm⁻². (b) Effect of discharge current on discharge capacity. Reprinted with permission from C. Xia et al., *Electrochem. Commun.* **26**, 93 (2013).

the mass of discharge products. For the electrode kinetics part, they used a Tafel equation with the transfer coefficient (or asymmetric factor) considered in the dependence of oxygen concentration. That is to say, the oxygen conversion rate was not simply assumed to be linearly dependent on the oxygen concentration in their model. Such is a key difference from previous models that assume an oxygen diffusion limited kinetics. In addition, the authors also carried out ab initio calculations on the electronic structures, especially the band gaps of various discharge products. These calculations are relevant since the authors identified the electronic passivation to be the key limitation on discharge, rather than pore clogging. Nevertheless, the ab initio results were not quantitatively related to the continuum model, since an empirical resistance formula for the discharge products were assumed.

Based on the similarity to the icing phenomenon in PEMFCs, Wang proposed another model in 2012[159] that takes into account the surface coverage of discharge products in LABs. In particular, he considered three different geometry of surface coverage: a cylindrical film growth mode just as in Sandhu's,[156] a spherical film growth mode just as in Albertus',[158] as well as a planar film growth mode. In either mode, an overpotential formula due to the grown thin film resistor has been derived. Moreover, the effect of reduced active surface area has been considered following a similar approach in fuel cells, which modifies the surface-to-volume ratio in the Butler-Volmer (actually Tafel in the paper) kinetic equation. It was also pointed out that an empirical formula for the tortuosity, as for each thin growth mode, should give better simulation results comparable to experiments, than using a constant tortuosity.

All the above models are isothermal 1D models. In an interesting work published in 2012,[165] Li and Faghri proposed a 2D non-isothermal model for lithium air batteries. The model is 2D in that a rib exists at the air inlet, which prevents some of the surface area from air exposure, but is actually required mechanically. Heat generation due to chemical reactions was considered, where the finite thermal conductivities of the positive electrode, the electrolyte and Li_2O_2 were involved. Heat flow from the air inlet was allowed. Besides the normal equation set similar to previous works, an extra heat conduction equation was involved. The authors discovered that the maximum temperature rise in the battery is less than 0.01 K even at their highest discharge current density, i.e., 0.5 mA/cm^2. This implies that temperature variation is generally not an issue in LAB modeling, due to the low current rate as well as the effective thermal exchange with the environment through the air inlet. Besides, they found that more Li_2O_2 was generated near the air inlet and most pores close to the separator were not utilized because of insufficient oxygen supply. This problem becomes even more severe at relatively higher current rates. To show how this can influence the cell design, they further simulated three cells with the same total porosity (0.75), but one with homogeneous porosity, one with more porosity near the air inlet and one with more porosity near the separator. In the latter two cells the porosity varies linearly across the positive electrode. The second cell has be largest discharge capacity as well as the largest cell voltage at each state of charge, while the third cell shows the opposite. This comparative study clearly shows the importance of the air inlet region which must be assigned more porosity such that the inner region of the positive electrode may get better oxygen supply. In other words, if the air inlet is clogged for oxygen transport, the inner region will not function even if it still has large porosity and large scope for discharge. Finally, the rib coverage effect was investigated, where an "open ratio" is defined as the part of inlet section that is not covered by the rib. When the open ratio degrades from 100% to 50%, the capacity also decreases from 529 mAh/g to 133 mAh/g. Therefore, the open ratio of the air inlet should be as large as possible.

Towards a Multiscale Model of Lithium Air Battery Operation

"Multiscale models" typically refer to models accounting for mathematical descriptions of mechanisms taking place at different spatial scales.[166] Multiscale models aim, by construction, to considerably re-

duce empirical assumptions than can be done in simple macroscopic models.

This is because they explicitly describe mechanisms in scales neglected in simple macroscopic models. Actually, multiscale models have a hierarchical structure: that means that solution variables defined in a lower hierarchy domain have finer spatial resolution than those solved in a higher hierarchy domain. Consequently, physical and chemical quantities of smaller length-scale physics are evaluated with a finer spatial resolution to resolve the impact of corresponding small-scale geometry. Larger-scale quantities are calculated with coarser spatial resolution, homogenizing the (possibly complex) smaller-scale geometric features. A multiscale model describes in this way physicochemical mechanisms occurring at multiple spatial scales with parameters which depend on the chemical and the structural properties of the materials, which are in turn pre-calculated at the atomistic and/or molecular level, expanding significantly the prediction capabilities of the standard macroscopic model.

These types of models have been already developed for other electrochemical systems such as PEMFCs. The main features of these models are that they can connect chemistry and structure of materials with electrochemical observables, thanks to the hierarchical combination between ab initio and CGMD generated databases and continuum models describing elementary kinetics and transport processes. Here we are intending to follow a similar approach for LABs. The following sections present a first stage in this attempt. Further details, numerical methods and a more complete model is in progress by us and will be published later.[167]

Our theory.— The key feature of our theory is the consideration of PSD. To emphasize this point, we have, in the following sections, neglected the Li^+ transport and solution phase resistance, but shall focus on the O_2 transport problem, together with a dynamically-variable reactive surface area. The theory is demonstrated in each scale as follows.

Macroscale.—The measurable potential of the cell is given by:

$$U_{cell} = U^+ - U^- \quad [8]$$

where U^+ and U^- are the potentials of the positive and the negative electrodes, respectively. They are defined as being the electrostatic potentials at the outmost external parts of the electrodes (*cf.* Fig. 17). In particular, U^+ is a time-dependent function of the competitive physicochemical mechanisms discussed in the next subsection. Potential U^- of the Li-foil is assumed to be governed by a symmetrical Butler-Volmer equation (in the inversed form):

$$U^- = \frac{2RT}{F} \sinh^{-1}\left(\frac{I}{2i_0 A_{Li}}\right) \quad [9]$$

where i_0 is the exchange current density and A_{Li} is the surface area of the negative electrode surface. Both the anodic and cathodic charge transfer coefficients are assumed to be 0.5. The equilibrium negative electrode potential at its solid-electrolyte interface, i.e., the equilibrium Li/Li$^+$ potential is defined to be zero as the global potential reference.
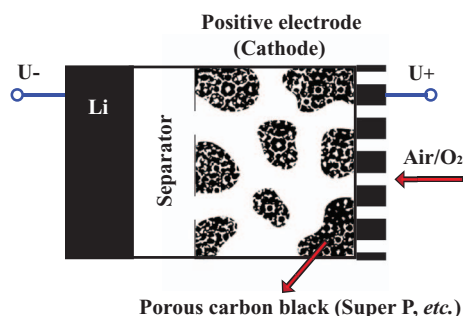

Figure 17. Schematics of our LAB model.

Table III. Oxygen Bunsen coefficient in various electrolyte solutions, quoted from J. Read et al., *J. Electrochem. Soc.* 150, A1351 (2003).[40]

Electrolyte	α	STD Dev%
1 M LiPF$_6$ PC:EC (1:1)	0.0482	13
1 M LiPF$_6$ PC	0.0516	14
1 M LiPF$_6$ PC:DME (1:1)	0.0722	2
1 M LiPF$_6$ PC:DMC (1:1)	0.0729	8
1 M LiPF$_6$ PC:DEC (1:1)	0.0787	6
1 M LiPF$_6$ PC:DME (1:2)	0.0998	2
0.5 M LiPF$_6$ PC:DME (1:2)	0.1218	4

The potential drop across the separator is given by:

$$\phi^+ - \phi^- = -I \times R_S \qquad [10]$$

where ϕ^+ and ϕ^- are the electrolyte potentials at the boundary between the separator and the positive and negative electrodes, respectively. R_S represents the separator resistance which can be a function of the operation temperature, and I the applied current. Detailed information on R_S depends on the transport model used in the mesoscale, as explained in the next subsection.

Mesoscale.—At the mesoscale, the transport of charges (Li$^+$, e$^-$), the reactants (O$_2$) and contaminant species (e.g. CO$_2$, H$_2$O) are described within the electrolyte filling the pores and across the electrode thickness. The most important transport process is that of oxygen, since the Bunsen coefficient of O$_2$ is very low in most organic solvents (some relevant data are shown in Table III from Read et al.). Hence, compared with Li$^+$ that is much more abundant, O$_2$ transport is much more likely to be the limiting factor. Neglecting the influence of CO$_2$ and H$_2$O, we model the transport of oxygen by Fick's law, possibly with a sink term in the positive electrode since O$_2$ is being consumed in electrode reactions.

$$\frac{\partial c_{O_2}}{\partial t} = \varepsilon^{1.5} (1-s)^{1.5} D \frac{\partial^2 c_{O_2}}{\partial x^2} - J_{O_2} \qquad [11]$$

Here ε is the porosity and s is the saturation, which is defined as

$$s = \frac{V_{Li_x O_y}}{V_e} \qquad [12]$$

where $V_{Li_x O_y}$ and V_e are the volumes of the discharge products and the electrolyte in a given region, respectively. The diffusion coefficient D is the ordinary diffusion coefficient of O$_2$ in intrinsic bulk solutions without any porous structure. The oxygen consumption flux density J_{O_2} is related to the faradaic current density by Faraday's law:

$$J_{O_2} = \frac{i}{2F} \qquad [13]$$

The coefficient 2 is due to the assumption of the electrode reaction below:

$$2Li^+ + 2e^- + O_2 \rightarrow Li_2O_2 \qquad [14]$$
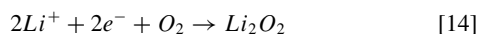
The electrode current density, when neglecting EDL charge/discharge, equals the faradaic current density. This current density is given by the Tafel equation, considering the overpotential in the positive electrode of LABs.

$$i = -2Fk \left(\frac{c_{Li^+}}{c_{Li^+}^{ref}} \right)^{2\beta} \left(\frac{c_{O_2}}{c_{O_2}^{ref}} \right)^{\beta} \exp\left(-\frac{2\beta F \eta}{RT} \right) \qquad [15]$$

Finally, the total current is an integral of current density over all surface areas of the positive electrode:

$$I = \int i \, da \qquad [16]$$

where we allow the surface area to vary over spatial locations, because the discharge products may reduce the available active surface area,

and that the current density distribution can be highly non-uniform due to the oxygen concentration variability within the positive electrode.

Among these governing equations, there are two parameters that are subject to dynamic update during simulations. The first one is the saturation, which is zero everywhere at the beginning of discharge. During discharge simulation, it is locally proportional to the total amount of Li$_2$O$_2$ precipitated. Since the solubility of Li$_2$O$_2$ is very low, we assume 100% precipitation, such that

$$s = \int_0^t \frac{a(t') M_{Li_2O_2} J_{O_2}(t')}{\rho_{Li_2O_2}} dt' \qquad [17]$$

where $a(t')$ is the specific reactive surface area at time t', $M_{Li_2O_2}$ and $\rho_{Li_2O_2}$ are the molar mass and density of Li$_2$O$_2$, respectively.

The reactive surface area a is the second dynamic parameter that changes its value during simulation. The detailed mechanism for reactive surface area degradation can be very complex. For example, small pores (several nanometers in diameter) are subject to being fully filled by discharge products, therefore losing all of their surface areas. Moreover, since the possible discharge products Li$_2$O$_2$, Li$_2$O and Li$_2$CO$_3$ are electronic insulators, there is probably a critical thickness for the oxide beyond which no electrons are available on the reaction plane that is close to the surface of the oxide. Therefore, carbon surface coated by such oxide film thicker than the critical value should be regarded as inactive. Finally, one can imagine that some pores, even large in their general size, may have merely a small entrance to the bulk of the electrolyte. Once this entrance is clogged by discharge products, a large inner surface area is lost because of the absence of continuous oxygen supply.

We model the electrode as a system consisting of multiple phases, each characterized by its volume fraction (a volume fraction being defined as the volume occupied by a single phase over the total electrode volume). Generally, the electrode composition is thus specified in terms of volume fractions of carbon (v_C), binder (v_{binder}), electrolyte (v_E), discharge products (v_{DP}) such as lithium oxides and other by-products like Li$_2$CO$_3$ from side reactions. The electrolyte volume fraction, through which the ionic transport takes place, is determined by

$$v_E = 1 - v_C - v_{binder} - v_{DP} = \varepsilon - v_{DP} \qquad [18]$$

As shown above, the parameter ε is regarded as the original porosity in the fully charged state, i.e., ε itself does not change during discharge, but only v_{DP} is subject to evolution.

Since the surface area and the pore volume have different relations to the pore radius (the former as r^2 while the later as r^3), the PSD information is required for deriving the surface area loss from the volume of discharge products. Various electrolyte-filled PSDs can be assumed for describing the electrode structure. For example a bi-modal log-normal distribution, a typical distribution found for carbons (e.g. Ketjen Black), normalized by the total volume fraction of electrolyte, can be adopted, in analogy to the previous theoretical work by Eikerling on liquid water transport in PEMFC:[56]

$$\frac{dv_E(r)}{dr} = \frac{\varepsilon - v_{DP}}{\sqrt{\pi} \{\ln(s_{PP}) + \chi_{SP} \ln(s_{SP})\}} \frac{1}{r}$$
$$\times \left\{ \exp\left(-\left(\frac{\ln\left(\frac{r}{r_{PP}}\right)}{\ln(s_{PP})} \right)^2 \right) + \chi_{SP} \exp\left(-\left(\frac{\ln\left(\frac{r}{r_{SP}}\right)}{\ln(s_{SP})} \right)^2 \right) \right\} \qquad [19]$$

The parameter χ_{SP} controls the relative contributions of primary and secondary pores, r_{PP} and r_{SP} determining the position of the two peaks, and s_{PP}, s_{SP} their widths.
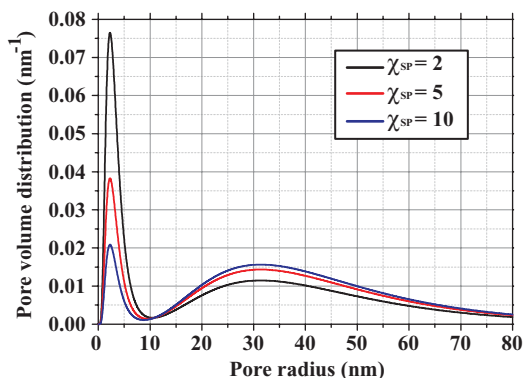
Figure 18. Demonstration of three PSD functions with different secondary-to-primary pore volume ratios.

Some PSDs are plotted in Fig. 18 for different χ_{SP} values, whilst the peak locations of the primary and secondary pores are kept the same.

Based on a proper-chosen PSD function, we here discuss the first case in the surface area loss mechanisms, where the decrease of active surface area is attributed to full filling of small pores. Nevertheless, still two possible mechanisms can be envisaged in this context. On the one hand, if the discharge products such as Li_2O_2 do not precipitate instantaneously, then the Kelvin equation indicates that the surface curvature has an influence on where the oxides will predominantly precipitate. Since common Li_2O_2/electrolyte interface has a negative surface tension,[168] Li_2O_2 prefers to precipitate in small pores that possess larger curvature. This implies that there is a critical radius r_C, below which all pores are filled by discharge products, but above which all pores are free of saturation. The parameter r_C may be derived by combining the PSD function with a mass conservation argument. Subsequently, the lost reactive surface area is found by integrating the area distribution function up to r_C. On the other hand, if the oxides precipitate locally, their thickness is proportional to the cumulative faradaic current flowed through this region. Reactive surface area lost may occur even when the oxide thickness is below the critical value, because each small pore will lose its surface area once the oxide thickness reaches its pore radius, which can be lower than the critical thickness. In this case the PSD function indicates the rate at which the filling of small pores occurs.

The model has been implemented within the computational framework provided by the simulation package MS LIBER-T (*Multiscale*
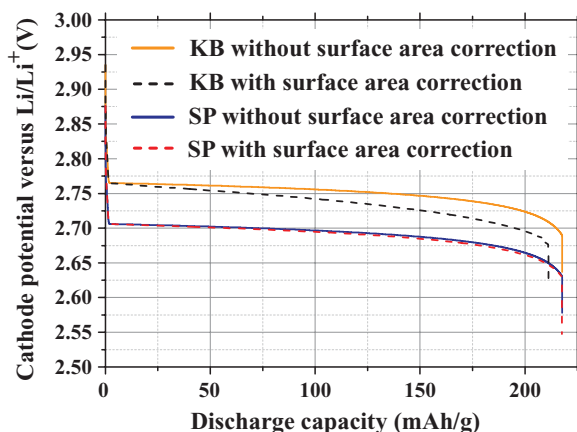
Simulator of Lithium Ion Batteries and Electrochemical Reactor Technologies), being developed at LRCS.[166,169]

First results.— Figure 19 demonstrates the discharge curves of a typical LAB at 0.5 mA/cm^2 rate. Two different carbons, i.e., Super P and Ketjen black are considered, with different PSD functions. For the Super P there are almost merely secondary pores, while for Ketjen black there are primary pores and secondary pores. The specific surface areas before discharge are 10^7 m^{-1} for Super P and 10^8 m^{-1} for Ketjen black. In the simulation, though the influence of saturation on O_2 transport is always considered, we on the other hand either considered the reactive surface area degradation phenomenon by the Kelvin equation approach, or neglect the change of active surface area. It can be seen that consideration of active surface area degradation has a prominent influence on the Ketjen black cell, but less on the Super P cell. This confirms that consideration of the PSD is necessary in developing LAB models.

Summary and Perspectives

Non-aqueous LABs are quite new electrochemical power generators which present very interesting theoretical features regarding their specific capacity and simplicity of operation principles. The use in these systems of inexpensive carbon-based positive electrodes is by itself interesting within a commercialization perspective. However, LABs are still far from a practical use as they suffer from poor cyclability and reversibility due to several irreversible phenomena including the incomplete release of lithium ions and oxygen during the charge process. The leading factors affecting the performance in real LAB positive electrodes and the mechanisms behind the ORR are still unclear. Physical theory and computational electrochemistry have a crucial role to play for fundamental understanding, diagnostics and design of new electrochemical materials and operation conditions for energy conversion and storage, as already demonstrated in the last 11 years.[61,62,78,84,96–98] However, in comparison to other electrochemical systems only very few mathematical models of LABs have been reported so far in literature. All these LAB models refer to macroscopic models having two main characteristics:

- they describe the global ORR kinetics on the basis of Butler-Volmer equations with parameters values (e.g. exchange-current, symmetry factors, etc.) fitted with experimental data. In that sense they do not rely on a detailed description of the elementary kinetic steps leading to the formation of lithium oxides, their morphology or the influence of metallic catalysts on the effectiveness of the reactions;
- they describe the O_2 transport across the porous electrode, accounting for the impact of the oxides growth onto the effective O_2 diffusion properties, but neglecting a detailed description of the micro and mesostructure of the electrode (e.g. the pore size distribution, and the propagation of the oxide dendrites inside the porous network).

While these models that are trained to experimental data provide already insights into the operation principles of LABs with easiness, due to their simple construction and fast computational speed, they possess several shortcomings. Specifically, the models are only as good as the experimental data they are trained to, and thereby do not provide the ability to extrapolate beyond the range of these data. In addition, changes in the cell design do not allow the use of the same models, and the task of building prototype cells, collecting data and training the model has to be repeated. More importantly, as these models are empirical in nature, they provide little, if any, deep insight into the operation principles of the cell in relation to the chemistry and structural properties of the used materials.

More efforts should be done in order to connect ab initio calculations with continuum models, even if ab initio approaches are also in the early stages of development for the case of LABs. These connections could facilitate the understanding of the elementary kinetics in ORR and OER during discharge and charge respectively, as well

Figure 19. Discharge simulation results for LABs with Ketjen black (KB) and Super P (SP) carbons at 0.5 mA/cm^2. The discharge curves with consideration of active surface area degradation are compared with those for which this effect is neglected.

as the electronic conductivity properties of the forming/decomposing lithium oxide layers.

Physical models should be further developed to capture the impact of the materials chemistry onto some effective properties essentially related to the electrochemical reactions and lithium ion transport. In particular, it is of key importance to clarify the role of catalysts onto the ORR/OER. Non-equilibrium thermodynamics phase field modeling approaches appear to be powerful techniques to understand lithium oxide phase formation and separation.

Electrode 3D reconstruction techniques, already being developed for LIBs,[170] should be imported to capture the impact of the "real" mesostructure (e.g. binder distribution) onto the local lithium reactivity and transport properties and the global cell efficiency. In particular, integrative multiphysics, multiscale and multiparadigm models spanning multiple scales and aiming to simulate competitions and synergies between electrochemical, transport, mechanical and thermal mechanisms should be developed.

Physical modeling has also a major role to play to clarify the impact of the electrolyte composition onto the performance and durability of LABs. Moreover, accurate modeling of the interfacial electrochemical reactions that combine chemistry with diffusion of radicals and formation of lithium carbonates and the solid electrolyte interphase (SEI) layer is an intrinsically multiscale problem, which is largely unaddressed.

The understanding of the LAB operation under pure and polluted air remains still a challenge as many chemical and electrochemical reactions could be involved in these processes.

Morphogenesis of the carbon electrodes as function of the ink properties and manufacture process (e.g. solvent used, deposition time, etc.), as well as the composition and structure of the SEI and its impact on the LAB capacity, should be further studied, e.g. by importing CGMD models already successfully applied for the simulation of complex materials mixtures in other systems such as PEMFCs. These models can predict the materials chemistry impact on their structure, and thus generate important parameters for continuum models.

A first model has been reported in this paper which allows capturing the impact of the pore size distribution on the discharge curves.

Other challenges recently described in a review paper on LIB multiscale modeling by Franco[166] are also fully applicable for LABs. Finally, to get progress on the development of multiscale models, it is crucial to develop multidisciplinarity between application domains. For example, computational scientists working in cosmology, geology and climate science could bring interesting methodological concepts for the widespread use of multiscale modeling in electrochemistry.

References

1. J. Goldstein, I. Brown, and B. Koretz, *J. Power Sources*, **80**, 171 (1999).
2. Q. Sun, Y. Yang, and Z.-W. Fu, *Electrochem. Commun.*, **16**, 22 (2012).
3. W. Li, C. Li, C. Zhou, H. Ma, and J. Chen, *Angew. Chem.*, **118**, 6155 (2006).
4. M. L. Doche, F. Novel-Cattin, R. Durand, and J. J. Rameau, *J. Power Sources*, **65**, 197 (1997).
5. P. Hartmann, C. L. Bender, M. Vračar, A. K. Dürr, A. Garsuch, J. Janek, and P. Adelhelm, *Nat. Mater.*, **12**, 228 (2013).
6. K. M. Abraham and Z. Jiang, *J. Electrochem. Soc.*, **143**, 1 (1996).
7. K. M. Abraham, *ECS Trans.*, **3**(42), 67 (2008).
8. G. Girishkumar, B. McCloskey, A. C. Luntz, S. Swanson, and W. Wilcke, *J. Phys. Chem. Lett.*, **1**, 2193 (2010).
9. F. Beck and P. Rüetschi, *Electrochim. Acta*, **45**, 2467 (2000).
10. Y. Shimonishi, T. Zhang, P. Johnson, N. Imanishi, A. Hirano, Y. Takeda, O. Yamamoto, and N. Sammes, *J. Power Sources*, **195**, 6187 (2010).
11. A. G. Ritchie, *J. Power Sources*, **96**, 1 (2001).
12. N. Imanishi, S. Hasegawa, T. Zhang, A. Hirano, Y. Takeda, and O. Yamamoto, *J. Power Sources*, **185**, 1392 (2008).
13. A. A. Franco, *ECS Trans.*, **6**(10), 1 (2007).
14. F. Li, H. Kitaura, and H. Zhou, *Energ. Environ. Sci.*, **6**, 2302 (2013).
15. B. Kumar, J. Kumar, R. Leese, J. P. Fellner, S. J. Rodrigues, and K. M. Abraham, *J. Electrochem. Soc.*, **157**, A50 (2010).
16. P. He, Y. Wang, and H. Zhou, *Electrochem. Commun.*, **12**, 1686 (2010).
17. J. Christensen, P. Albertus, R. S. Sanchez-Carrera, T. Lohmann, B. Kozinsky, R. Liedtke, J. Ahmed, and A. Kojic, *J. Electrochem. Soc.*, **159**, R1 (2012).
18. A. Oberlin, High resolution TEM studies of carbonization and graphitization, in: P. A. Thrower (Ed.), *Chemistry and Physics of Carbon*, Vol. 22, pp. 1–144, Marcel Dekker, New York, USA (1989).
19. J. D. Bernal, *Proc. R. Soc. Lond. A.*, **106**, 749 (1924).
20. B. McEnaney, *Carbon*, **26**, 267 (1988).
21. T. Ogasawara, A. Débart, M. Holzapfel, P. Novák, and P. G. Bruce, *J. Am. Chem. Soc.*, **128**, 1390 (2006).
22. X. Ren, S. S. Zhang, D. T. Tran, and J. Read, *J. Mater. Chem.*, **21**, 10118 (2011).
23. Y.-C. Lu, Z. Xu, H.A. Gasteiger, S. Chen, K. Hamad-Schifferli, and Y. Shao-Horn, *J. Am. Chem. Soc.*, **132**, 12170 (2010).
24. S. D. Beattie, D. M. Manolescu, and S. L. Blair, *J. Electrochem. Soc.*, **156**, A44 (2009).
25. O. Crowther, B. Meyer, M. Morgan, and M. Salomon, *J. Power Sources*, **196**, 1498 (2011).
26. J.-G. Zhang, D. Wang, W. Xu, J. Xiao, and R. E. Williford, *J. Power Sources*, **195**, 4332 (2010).
27. Y. Li, J. Wang, X. Li, J. Liu, D. Geng, J. Yang, R. Li, and X. Sun, *Electrochem. Commun.*, **13**, 668 (2011).
28. J. Dai, T. Kogut, L. Jin, and D. Reisner, *ECS Trans.*, **6**(25), 381 (2008).
29. X.-h. Yang, P. He, and Y.-y. Xia, *Electrochem. Commun.*, **11**, 1127 (2009).
30. M. Mirzaeian and P.J. Hall, *Power System Technology (Beijing)*, **31**, 90 (2007).
31. M. Mirzaeian and P.J. Hall, *Electrochim. Acta*, **54**, 7444 (2009).
32. M. Mirzaeian and P.J. Hall, *J. Power Sources*, **195**, 6817 (2010).
33. E. Yoo and H. Zhou, *ACS nano*, **5**, 3020 (2011).
34. Y. Wang and H. Zhou, *Energ. Environ. Sci.*, **4**, 1704 (2011).
35. Y. Li, J. Wang, X. Li, D. Geng, R. Li, and X. Sun, *Chem. Commun.*, **47**, 9438 (2011).
36. C. K. Park, S. B. Park, S. Y. Lee, H. Lee, H. Jang, and W. I. Cho, *Bull. Korean Chem. Soc.*, **31**, 3221 (2010).
37. Z. Peng, S. A. Freunberger, Y. Chen, and P. G. Bruce, *Science*, **337**, 563 (2012).
38. S. A. Freunberger, Y. Chen, Z. Peng, J. M. Griffin, L. J. Hardwick, F. Bardé, P. Novák, and P. G. Bruce, *J. Am. Chem. Soc.*, **133**, 8040 (2011).
39. L.-L. Zhang, Z.-L. Wang, D. Xu, X.-B. Zhang, and L.-M. Wang, *International Journal of Smart and Nano Materials*, **4**, 27 (2013).
40. J. Read, K. Mutolo, M. Ervin, W. Behl, J. Wolfenstine, A. Driedger, and D. Foster, *J. Electrochem. Soc.*, **150**, A1351 (2003).
41. A. Débart, A. J. Paterson, J. Bao, and P. G. Bruce, *Angew. Chem. Int. Ed it.*, **47**, 4521 (2008).
42. W. Xu, J. Xiao, J. Zhang, D. Wang, and J.-G. Zhang, *J. Electrochem. Soc.*, **156**, A773 (2009).
43. J. Xiao, D. Wang, W. Xu, D. Wang, R. E. Williford, J. Liu, and J.-G. Zhang, *J. Electrochem. Soc.*, **157**, A487 (2010).
44. T. Kuboki, T. Okuyama, T. Ohsaki, and N. Takami, *J. Power Sources*, **146**, 766 (2005).
45. J. Xiao, W. Xu, D. Wang, and J.-G. Zhang, *J. Electrochem. Soc.*, **157**, A294 (2010).
46. A. Débart, J. Bao, G. Armstrong, and P. G. Bruce, *J. Power Sources*, **174**, 1177 (2007).
47. A. K. Thapa and T. Ishihara, *J. Power Sources*, **196**, 7016 (2011).
48. A. K. Thapa, K. Saimen, and T. Ishihara, *Electrochem. Solid-State Lett.*, **13**, A165 (2010).
49. R. R. Mitchell, B. M. Gallant, C. V. Thompson, and Y. Shao-Horn, *Energ. Environ. Sci.*, **4**, 2952 (2011).
50. F. Mizuno, S. Nakanishi, Y. Kotani, S. Yokoishi, and H. Iba, *Electrochemistry*, **78**, 403 (2010).
51. B. D. McCloskey, D. S. Bethune, R. M. Shelby, G. Girishkumar, and A. C. Luntz, *J. Phys. Chem. Lett.*, **2**, 1161 (2011).
52. J. Xiao, J. Hu, D. Wang, D. Hu, W. Xu, G. L. Graff, Z. Nie, J. Liu, and J.-G. Zhang, *J. Power Sources*, **196**, 5674 (2011).
53. G. Girishkumar, B. McCloskey, A. C. Luntz, S. Swanson, and W. Wilcke, *J. Phys. Chem. Lett.*, **1**, 2193 (2010).
54. C. Tran, X.-Q. Yang, and D. Qu, *J. Power Sources,* **195**, 2057 (2010).
55. D. Zheng, H.-S. Lee, X.-Q. Yang, and D. Qu, *Electrochem. Commun.*, **28**, 17 (2013).
56. M. Eikerling, *J. Electrochem. Soc.*, **153**, E58 (2006).
57. K. Takechi, T. Shiga, and T. Asaoka, *Chem. Commun.*, **47**, 3463 (2011).
58. S. R. Gowda, A. Brunet, G. M. Wallraff, and B. D. McCloskey, *J. Phys. Chem. Lett.*, **4**, 276 (2013).
59. S. Meini, M. Piana, N. Tsiouvaras, A. Garsuch, and H. A. Gasteiger, *Electrochem. Solid-State Lett.*, **15**, A45 (2012).
60. A. A. Franco, PEMFC degradation modeling and analysis, in: C. Hartnig and C. Roth (Eds.), *Polymer electrolyte membrane and direct methanol fuel cell technology (PEMFCs and DMFCs)*, Volume 1: Fundamentals and performance, Woodhead, UK (2012).
61. A. A. Franco (Ed.), *Polymer Electrolyte Fuel Cells: Science, Applications and Challenges*, CRC Press, Taylor and Francis group, FL, USA (2013).

62. A. A. Franco, M. Guinard, B. Barthe, and O. Lemaire, *Electrochim. Acta*, **54**, 5267 (2009).
63. V. Parry, G. Berthomé, J.-C. Joud, O. Lemaire, and A. A. Franco, *J. Power Sources*, **196**, 2530 (2011).
64. X. Cheng, Z. Shi, N. Glass, L. Zhang, J. Zhang, D. Song, Z.-S. Liu, H. Wang, and J. Shen, *J. Power Sources*, **165**, 739 (2007).
65. E. Dy, Z. Shi, K. Fatih, J. Zhang, and Z.-S. Liu, in: A. A. Franco (Ed.), *Polymer Electrolyte Fuel Cells: Science, Applications and Challenges*, CRC Press, Taylor and Francis group, FL, USA (2013).
66. J. Read, *J. Electrochem. Soc.*, **149**, A1190 (2002).
67. H. Cheng and K. Scott, *J. Power Sources*, **195**, 1370 (2010).
68. G. Q. Zhang, J. P. Zheng, R. Liang, C. Zhang, B. Wang, M. Hendrickson, and E. J. Plichta, *J. Electrochem. Soc.*, **157**, A953 (2010).
69. C.-J. Lan, Y.-F. Chi, and T.-S. Chin, *ECS Trans.*, **3**(42), 51 (2008).
70. S. R. Younesi, S. Urbonaite, F. Björefors, and K. Edström, *J. Power Sources*, **196**, 9835 (2011).
71. N.-S. Choi, Z. Chen, S. A. Freunberger, X. Ji, Y.-K. Sun, K. Amine, G. Yushin, L. F. Nazar, J. Cho, and P. G. Bruce, *Angew. Chem. Int. Edit.*, **51**, 9994 (2012).
72. A. Kraytsberg and Y. Ein-Eli, *J. Power Sources*, **196**, 886 (2011).
73. J. Hou, M. Yang, M. W. Ellis, R. B. Moore, and B. Yi, *Phys. Chem. Chem. Phys.*, **14**, 13487 (2012).
74. D. Beeman, J. Silverman, R. Lynds, and M. R. Anderson, *Physical Review B*, **30**, 870 (1984).
75. http://www.geodict.com/.
76. K. Malek, M. Eikerling, Q. Wang, T. Navessin, and Z. Liu, *J. Phys. Chem. C*, **111**, 13627 (2007).
77. H. Friedrich, P. E. de Jongh, A. J. Verkleij, and K. P. de Jong, *Chem. Rev.*, **109**, 1613 (2009).
78. K. Malek and A. A. Franco, *J. Phys. Chem. B*, **115**, 8088 (2011).
79. K. Malek, T. Mashio, and M. Eikerling, *Electrocatalysis*, **2**, 141 (2011).
80. C. Merlet, B. Rotenberg, P. A. Madden, P.-L. Taberna, P. Simon, Y. Gogotsi, and M. Salanne, *Nat. Mater.*, **11**, 306 (2012).
81. Y. Xu and W. A. Shelton, *J. Electrochem. Soc.*, **158**, A1177 (2011).
82. J. Xiao, D. Mei, X. Li, W. Xu, D. Wang, G. L. Graff, W. D. Bennett, Z. Nie, L. V. Saraf, I. A. Aksay, J. Liu, and J.-G. Zhang, *Nano Lett.*, **11**, 5071 (2011).
83. G. Henkelman, B. P. Uberuaga, and H. Jónsson, *J. Chem. Phys.*, **113**, 9901 (2000).
84. R. F. de Morais, P. Sautet, D. Loffreda, and A. A. Franco, *Electrochim. Acta*, **56**, 10842 (2011).
85. H. Cheng and K. Scott, *Appl. Catal. B-E nviron.*, **108–109**, 140 (2011).
86. B. D. McCloskey, R. Scheffler, A. Speidel, D. S. Bethune, R. M. Shelby, and A. C. Luntz, *J. Am. Chem. Soc.*, **133**, 18038 (2011).
87. T. Jacob and W. A. Goddard, *ChemPhysChem*, **7**, 992 (2006).
88. Y. Wang and P. B. Balbuena, *J. Chem. Theory Comput.*, **1**, 935 (2005).
89. T. Jacob, *Fuel Cells*, **6**, 159 (2006).
90. B. C. Han, C. R. Miranda, and G. Ceder, *Phys. Rev. B*, **77**, 075410 (2008).
91. L. Wang, A. Roudgar, and M. Eikerling, *J. Phys. Chem. C*, **113**, 17989 (2009).
92. A. Roudgar, M. Eikerling, and R. van Santen, *Phys. Chem. Chem. Phys.*, **12**, 614 (2010).
93. Y. Wang and P. B. Balbuena, *J. Phys. Chem. B*, **108**, 4376 (2004).
94. T. Jacob and W. A. Goddard, *J. Am. Chem. Soc.*, **126**, 9360 (2004).
95. J. K. Nørskov, J. Rossmeisl, A. Logadottir, L. Lindqvist, J. R. Kitchin, T. Bligaard, and H. Jónsson, *J. Phys. Chem. B*, **108**, 17886 (2004).
96. L. F. L. Oliveira, S. Laref, E. Mayousse, C. Jallut, and A. A. Franco, *Phys. Chem. Chem. Phys.*, **14**, 10215 (2012).
97. A. A. Franco, S. Passot, P. Fugier, C. Anglade, E. Billy, L. Guétaz, N. Guillet, E. De Vito, and S. Mailley, *J. Electrochem. Soc.*, **156**, B410 (2009).
98. A. A. Franco, P. Schott, C. Jallut, and B. Maschke, *Fuel Cells*, **7**, 99 (2007).
99. A. A. Franco, P. Schott, C. Jallut, and B. Maschke, *J. Electrochem. Soc.*, **153**, A1053 (2006).
100. R. Subbaraman, D. Strmcnik, V. Stamenkovic, and N. M. Markovic, *J. Phys. Chem. C*, **114**, 8414 (2010).
101. A. A. Franco, M. Quiroga, R. F. de Morais, D. Loffreda, and P. Sautet, to be submitted (2013).
102. G. Galli, R. M. Martin, R. Car, and M. Parrinello, *Phys. Rev. Lett.*, **62**, 555 (1989).
103. R. D. Heidenreich, W. M. Hess, and L. L. Ban, *J. Appl. Crystallogr.*, **1**, 1 (1968).
104. D. Pantea, H. Darmstadt, S. Kaliaguine, L. Sümmchen, and C. Roy, *Carbon*, **39**, 1147 (2001).
105. J. Lahaye and F. Ehrburger-Dolle, *Carbon*, **32**, 1319 (1994).
106. F. Fehér, I. von Wilucki, and G. Dost, *Chemische Berichte*, **86**, 1429 (1953).
107. H. Föppl, *Zeitschrift für Anorganische und Allgemeine Chemie*, **291**, 12 (1957).
108. L. G. Cota and P. de la Mora, *Acta Crystallogr. Sect. B*, **61**, 133 (2005).
109. M. K. Y. Chan, E. L. Shirley, N. K. Karan, M. Balasubramanian, Y. Ren, J. P. Greeley, and T. T. Fister, *J. Phys. Chem. Lett.*, **2**, 2483 (2011).
110. H. Y. Wu, H. Zhang, X. L. Cheng, and L. C. Cai, *Phys. Lett. A*, **360**, 352 (2006).
111. M. D. Radin, J. F. Rodriguez, F. Tian, and D. J. Siegel, *J. Am. Chem. Soc.*, **134**, 1093 (2012).
112. W. E. Pickett and J. S. Moodera, *Phys. Today*, **54**, 39 (2001).
113. M. D. Radin, F. Tian, and D. J. Siegel, *J. Mater. Sci.*, **47**, 7564 (2012).
114. J. P. Perdew, K. Burke, and M. Ernzerhof, *Phys. Rev. Lett.*, **77**, 3865 (1996).
115. J. Heyd, G. E. Scuseria, and M. Ernzerhof, *J. Chem. Phys.*, **118**, 8207 (2003).
116. J. Heyd, G. E. Scuseria, and M. Ernzerhof, *J. Chem. Phys.*, **124**, 219906 (2006).
117. L. Hedin, *Phys. Rev.*, **139**, A796 (1965).
118. S. P. Ong, Y. Mo, and G. Ceder, *Phys. Rev. B*, **85**, 081105 (2012).
119. J. M. Garcia-Lastra, J. S. G. Myrdal, R. Christensen, K. S. Thygesen, and T. Vegge, *J. Phys. Chem. C*, in press (2013).
120. P. Albertus, G. Girishkumar, B. McCloskey, R. S. Sánchez-Carrera, B. Kozinsky, J. Christensen, and A. C. Luntz, *J. Electrochem. Soc.*, **158**, A343 (2011).
121. O. Gerbig, R. Merkle, and J. Maier, *Adv. Mater.*, **25**, 3129 (2013).
122. L. Wang, T. Maxisch, and G. Ceder, *Phys. Rev. B*, **73**, 195107 (2006).
123. G. Kresse and J. Furthmüller, *Comput. Mater. Sci.*, **6**, 15 (1996); *Phys. Rev. B*, **54**, 11169 (1996).
124. G. Kresse and J. Furthmüller, *Phys. Rev. B*, **54**, 11169 (1996).
125. N. Seriani, *Nanotechnology*, **20**, 445703 (2009).
126. K. McKenna, A. Shluger, V. Iglesias, M. Porti, M. Nafría, M. Lanza, and G. Bersuker, *Microelectron. Eng.* **88**, 1272 (2011).
127. G. Bersuker, D. C. Gilmer, D. Veksler, P. Kirsch, L. Vandelli, A. Padovani, L. Larcher, K. McKenna, A. Shluger, V. Iglesias, M. Porti, and M. Nafría, *J. Appl. Phys.*, **110**, 124518 (2011).
128. K.-H. Xue, P. Blaise, L. R. C. Fonseca, G. Molas, E. Vianello, B. Traoré, B. De Salvo, G. Ghibaudo, and Y. Nishi, *Appl. Phys. Lett.*, **102**, 201908 (2013).
129. G. K. Singh, G. Ceder, and M. Z. Bazant, *Electrochim. Acta*, **53**, 7599 (2008).
130. P. Bai, D. A. Cogswell, and M. Z. Bazant, *Nano Lett.*, **11**, 4890 (2011).
131. D. A. Cogswell and M. Z. Bazant, *ACS Nano*, **6**, 2215 (2012).
132. J. W. Cahn and J. E. Hilliard, *J. Chem. Phys.*, **28**, 258 (1958).
133. J. E. Guyer, W. J. Boettinger, J. A. Warren, and G. B. McFadden, *Phys. Rev. E*, **69**, 021603 (2004).
134. J. E. Guyer, W. J. Boettinger, J. A. Warren, and G. B. McFadden, *Phys. Rev. E*, **69**, 021604 (2004).
135. B. C. Han, A. Van der Ven, D. Morgan, and G. Ceder, *Electrochim. Acta*, **49**, 4691 (2004).
136. A. J. Bray, *Adv. Phys.*, **43**, 357 (1994).
137. T. K. Nguyen, K.-H. Xue, Y. Mammeri, J. P. Chehab, and A. A. Franco, in preparation.
138. J. S. Hummelshøj, J. Blomqvist, S. Datta, T. Vegge, J. Rossmeisl, K. S. Thygesen, A. C. Luntz, K. W. Jacobsen, and J. K. Nørskov, *J. Chem. Phys.*, **132**, 071101 (2010).
139. M. Doyle, T. F. Fuller, and J. Newman, *J. Electrochem. Soc.*, **140**, 1526 (1993).
140. T. F. Fuller, M. Doyle, and J. Newman, *J. Electrochem. Soc.*, **141**, 1 (1994).
141. W. Lai and F. Ciucci, *Electrochim. Acta*, **56**, 4369 (2011).
142. F. Ciucci and W. Lai, *Transp ort Porous Med.*, **88**, 249 (2011).
143. D. Gillespie, W. Nonner, and R. S. Eisenberg, *J. Phys .: Condens. Mat.*, **14**, 12129 (2002).
144. J. Newman and K. E. Thomas-Alyea, *Electrochemical systems*, 4th Edition, Wiley-Interscience (2012).
145. K.-H. Xue and G. L. Plett, *Electrochimica Acta*, **87**, 575 (2013).
146. A. Latz and J. Zausch, *J. Power Sources*, **196**, 3296 (2011).
147. K. Henjes and M. Liu, *Annals of Physics*, **223**, 243 (1993).
148. M. Liu, *Phys. Rev. Lett.*, **70**, 3580 (1993).
149. M. M. Ottakam Thotiyl, S. A. Freunberger, Z. Peng, and P. G. Bruce, *J. Am. Chem. Soc.*, **135**, 494 (2012).
150. A. A. Franco and K.-H. Xue, in preparation (2013).
151. D. A. G. Bruggeman, *Annalen der Physik*, **416**, 636 (1935).
152. M. Doyle, J. Newman, A. S. Gozdz, C. N. Schmutz, and J.-M. Tarascon, *J. Electrochem. Soc.*, **143**, 1890 (1996).
153. G. Sikha, B. N. Popov, and R. E. White, *J. Electrochem. Soc.*, **151**, A1104 (2004).
154. I. Kowalczk, J. Read, and M. Salomon, *Pure Appl. Chem.*, **79**, 851 (2007).
155. J. Read, K. Mutolo, M. Ervin, W. Behl, J. Wolfenstine, A. Driedger, and D. Foster, *J. Electrochem. Soc.*, **150**, A1351 (2003).
156. S. S. Sandhu, J. P. Fellner, and G. W. Brutchen, *J. Power Sources*, **164**, 365 (2007).
157. P. Andrei, J. P. Zheng, M. Hendrickson, and E. J. Plichta, *J. Electrochem. Soc.*, **157**, A1287 (2010).
158. P. Albertus, G. Girishkumar, B. McCloskey, R. S. Sánchez-Carrera, B. Kozinsky, J. Christensen, and A. C. Luntz, *J. Electrochem. Soc.*, **158**, A343 (2011).
159. Y. Wang, *Electrochim. Acta*, **75**, 239 (2012).
160. E. Breitbarth, M. M. Mills, G. Friedrichs, and J. LaRoche, *Limnology and Oceanography: Methods*, **2**, 282 (2004).
161. J. Newman, *Chem. Eng. Sci.*, **64**, 4796 (2009).
162. C. Xia, C. L. Bender, B. Bergner, K. Peppler, and J. Janek, *Electrochem. Commun.*, **26**, 93 (2013).
163. L. Pisani, *Int. J. Heat Mass Transf.*, **51**, 650 (2008).
164. J. P. Zheng, R. Y. Liang, M. Hendrickson, and E. J. Plichta, *J. Electrochem. Soc.*, **155**, A432 (2008).
165. X. Li and A. Faghri, *J. Electrochem. Soc.*, **159**, A1747 (2012).
166. A. A. Franco, *RSC Adv.*, **3**, 13027 (2013).
167. K.-H. Xue and A. A. Franco, in preparation.
168. V. Y. Nimon, S. J. Visco, L. C. De Jonghe, Y. M. Volfkovich, and D. A. Bograchev, *ECS Electrochem. Lett.*, **2**, A33 (2013).
169. http://www.modeling-electrochemistry.com.
170. M. Ender, J. Joos, T. Carraro, and E. Ivers-Tiffée, *Electrochem. Commun.*, **13**, 166 (2011).